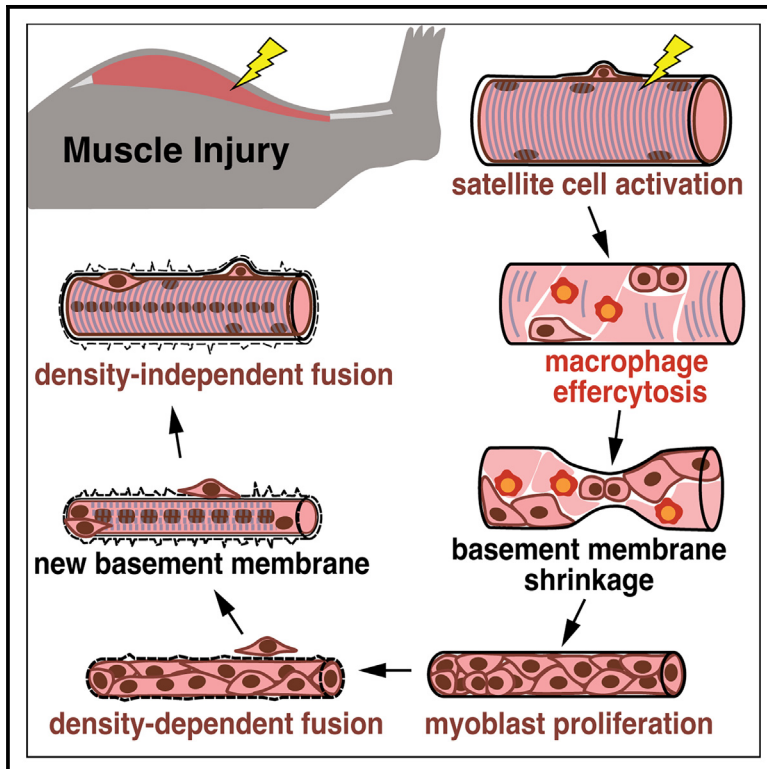# Developmental Cell

Three-dimensional imaging studies in mice identify cellular dynamics of skeletal muscle regeneration

Graphical abstract

Authors

Brittany C. Collins, Jacob B. Shapiro,
Mya M. Scheib, Robert V. Musci,
Mayank Verma, Gabrielle Kardon

Correspondence

gkardon@genetics.utah.edu

In brief

Collins and Shapiro et al. reconstruct muscle regeneration in three dimensions, showing that myofibers form via two waves of fusion: density-dependent myocyte fusion, within residual basement membrane tubes of necrotic myofibers, establishes correctly oriented myofibers, while myocyte-myofiber fusion enlarges them. Surprisingly, centralized myonuclei are an enduring feature of regenerated myofibers.

Highlights

- Myocyte-myocyte fusion establishes myofibers, then myocyte-myofiber fusion enlarges them

- Residual myofiber basement membrane promotes fusion and orients regenerated myofibers

- Macrophage debris clearance is essential for fusion and formation of linear myofibers

- Centralized myonuclei of regenerated myofibers are present for $\geq$10 months post injury

CelPress

Developmental Cell

 CellPress

Article

Three-dimensional imaging studies in mice identify cellular dynamics of skeletal muscle regeneration

Brittany C. Collins,[1,3,4] Jacob B. Shapiro,[1,3,5] Mya M. Scheib,[1] Robert V. Musci,[1,6] Mayank Verma,[2] and Gabrielle Kardon[1,7,*]

[1]Department of Human Genetics, University of Utah, Salt Lake City, UT, USA
[2]Department of Pediatrics, Division of Neurology, University of Texas Southwestern Medical Center, Dallas, TX, USA
[3]These authors contributed equally
[4]Present address: BioFire Defense, Murray, UT, USA
[5]Present address: Department of Anesthesiology, University of Wisconsin School of Medicine and Public Health, Madison, WI, USA
[6]Present address: Department of Health and Human Sciences, Frank R Seaver College of Science and Engineering, Loyola Marymount University, Los Angeles, CA, USA
[7]Lead contact
*Correspondence: gkardon@genetics.utah.edu
https://doi.org/10.1016/j.devcel.2024.03.017

SUMMARY

The function of many organs, including skeletal muscle, depends on their three-dimensional structure. Muscle regeneration therefore requires not only reestablishment of myofibers but also restoration of tissue architecture. Resident muscle stem cells (SCs) are essential for regeneration, but how SCs regenerate muscle architecture is largely unknown. We address this problem using genetic labeling of mouse SCs and whole-mount imaging to reconstruct, in three dimensions, muscle regeneration. Unexpectedly, we found that myofibers form via two distinct phases of fusion and the residual basement membrane of necrotic myofibers is critical for promoting fusion and orienting regenerated myofibers. Furthermore, the centralized myonuclei characteristic of regenerated myofibers are associated with myofibrillogenesis and endure months post injury. Finally, we elucidate two cellular mechanisms for the formation of branched myofibers, a pathology characteristic of diseased muscle. We provide a synthesis of the cellular events of regeneration and show that these differ from those used during development.
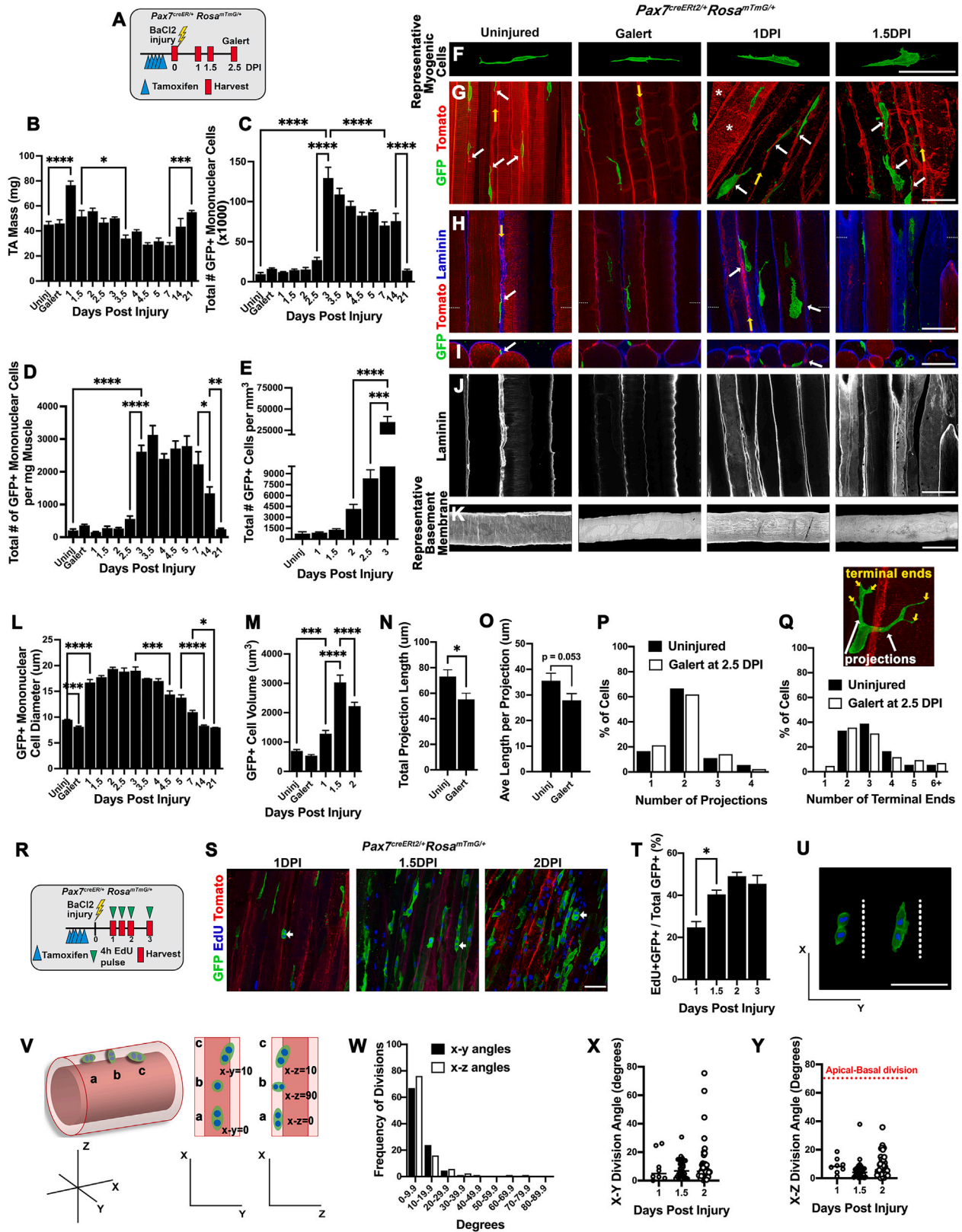
INTRODUCTION

Stem cells (SCs) are critical for the regeneration of a variety of tissues. These cells are characterized by their ability to self-renew and to differentiate and regenerate tissue.[1] To repair three-dimensionally complex tissues, SCs must not only differentiate but also need to restore tissue architecture. Although the molecular and cellular processes regulating SC self-renewal and differentiation have been intensely studied, how SCs regenerate tissue architecture is largely unknown. Here, we examine *in vivo* how SCs regenerate the architecture of a three-dimensionally complex tissue, skeletal muscle.

Adult vertebrate skeletal muscle is composed of multinucleate post-mitotic myofibers. In response to injury or damage, a tissue resident population of dedicated muscle SCs, originally termed satellite cells,[2–5] are necessary and sufficient for muscle regeneration.[6–8] In uninjured muscle, quiescent SCs reside in a "satellite" niche between the sarcolemma and the basement membrane (BM) of the myofiber.[5] The BM is a sheath of extracellular matrices, notably including laminin, that surrounds the basal aspect of myofibers.[9] Upon muscle injury, SCs activate and re-

enter the cell cycle. Asymmetric cell division of activated SCs is thought to establish the subsequent fate of SCs to either self-renew or differentiate into myofibers.[10–12] SCs destined to regenerate myofibers become committed myoblasts, differentiate into myocytes, and fuse to reestablish myofibers.[13]

SCs not only undergo myogenesis but also regenerate the three-dimensional muscle architecture, with each anatomical muscle having a unique organization and orientation of myofibers. After most forms of muscle injury, regeneration yields muscles with correctly oriented and aligned myofibers.[14,15] Histological and electron micrograph studies have suggested that the residual BM of necrotic myofibers is important for ensuring proper alignment of regenerated myofibers,[14,16–19] but these techniques lack the three-dimensional view required to reveal the complete regenerative process at the tissue level. Also essential for optimal muscle function is the regeneration of linear, as opposed to branched, myofibers—as the latter are associated with impaired contractile activity and are more susceptible to damage.[20–23] Branched myofibers are characteristic of dystrophic muscle[23–30] and are found with a higher incidence after regeneration[28,31] and with age.[28] However, the mechanisms

(legend on next page)

Developmental Cell
Article

CellPress

that ensure production of linear versus branched regenerated myofibers are still unclear. Finally, it has long been recognized that the cytoarchitecture of regenerated myofibers is distinct from uninjured myofibers; regenerated myofibers have chains of centralized myonuclei, while uninjured myofibers have regularly spaced peripheral nuclei.[32–35] How these centralized myonuclei arise during regeneration and whether (and how) these central nuclei move peripherally as regenerated myofibers mature are still outstanding questions.[33,34,36–38]

The cellular events of regeneration are often suggested to closely mirror development.[39,40] The ultimate result of muscle development and regeneration is the creation of functional skeletal muscles. For the most part, the structure and function of developed and regenerated muscles look similar. However, there are some key differences, principally the organization of myonuclei.[32–35] These morphological differences suggests that myogenesis may differ between regeneration and development.

In this study, using genetic labeling of mouse SCs and imaging and reconstruction of muscle in whole mount, we determine how SCs regenerate the three-dimensional architecture of skeletal muscle after myofiber destruction. We provide a synthesis of the cellular events leading to regeneration and reveal key differences between development and regeneration of skeletal muscle.

RESULTS

Three-dimensional visualization and quantification of myogenic cells during regeneration

To investigate SCs and their progeny during muscle regeneration *in vivo*, we optimized a previously published whole-mount tissue-clearing technique[41] that allows for the three-dimensional visualization of the cellular processes of regeneration. We used a $Pax7^{CreERT2}$ allele that specifically and efficiently induces Cre-mediated recombination in SCs following tamoxifen (TAM) delivery.[7] These mice were crossed to the $Rosa^{mTmG}$ reporter, which, in the absence of Cre, ubiquitously expresses membrane-bound Tomato (TOM), but in the presence of Cre, Pax7+ cells and their

progeny express membrane-bound GFP-[42]. $Pax7^{CreERT2/+}$; $Rosa^{mTmG/+}$ mice were used in all studies unless otherwise stated. We focused on regeneration of the tibialis anterior (TA) and extensor digitorum longus (EDL) muscles, whose myofibers are aligned parallel to one another and to the limb's long axis. We genetically labeled SCs and their progeny with GFP via TAM, injured both TA and EDL muscles via intramuscular injection of BaCl2, and harvested muscles at various days post injury (DPI; Figure 1A). BaCl2 leads to acute damage of myofibers via cell membrane depolarization, hypercontraction, proteolysis, and membrane rupture.[44] TAs were weighed and processed for fluorescence activated cell sorting (FACS) of SCs (gating strategy in Figure S1), while EDLs were processed for whole-mount imaging.

BaCl2 injury led to a transient increase, subsequent decline, and then recovery in muscle mass by 21 DPI (Figure 1B). To assess the overall effect of injury on SCs and their progeny we analyzed the number of mononuclear myogenic cells. By FACS and quantification of GFP+ myogenic cells in whole-mount images, we found that there was a rapid increase in mononuclear myogenic cells between 2.5 and 3 DPI (Figures 1C–1E). High numbers of mononuclear myogenic cells were present through 14 DPI and then declined as myogenic cells fused to make myofibers or returned to quiescence (Figures 1C and 1D). Given this framework, we proceeded to analyze in whole mount the cellular processes by which SCs regenerate myofibers.

Quiescent, Galert, and newly activated SCs are distinct in morphology and size

To visualize quiescent SCs in their distinct niche[5,12,45,46] *in vivo*, we imaged perfused, fixed whole-mount uninjured EDLs by confocal microscopy and reconstructed their three-dimensional structure with Fluorender (Figures 1F–1K; Video S1).[47] In these muscles, TOM labeled all uninjured myofibers (Figures 1G and 1H)[48] and capillaries lying between myofibers (yellow arrows, Figures 1G and 1H). Other cell types, such as fibroadipogenic progenitors (FAPs), were labeled at much lower levels with TOM than myofibers and capillaries and are therefore not shown. We found

Figure 1. Quiescent, Galert, and activated SCs are distinct in size and shape, and activated SCs proliferate via planar divisions within residual BM tubes

(A) Experimental design for labeling SCs, 0–1.5 DPI, and Galert (2.5 DPI contralateral uninjured EDL).

(B) TA mass during regeneration (n = 3–5 mice/DPI).

(C–E) Number of GFP+ mononuclear myogenic cells in TA by FACS (n = 3–5 mice/DPI) (C and D) and counts on whole-mount images of EDLs (n = 3–7 mice/DPI) (E).

(F–K) Whole-mount images of uninjured, Galert, and 1 and 1.5 DPI EDL (n ≥ 3 mice/DPI). (F) Representative segmented SCs. (G and H) Superficial view of GFP+ SCs and TOM+ uninjured myofibers (uninjured and Galert columns), TOM+ degrading myofibers (*s at 1 DPI), and TOM+ capillaries (all columns). (H) Laminin+ BM outlines uninjured myofibers, residual BM of injured myofibers, and surrounds capillaries. Dotted white lines indicate cross-section level shown in (I). White arrows in (G)–(I) show GFP+ SCs in close contact with TOM+ capillaries. Yellow arrows in (G) and (H) show representative TOM+ capillaries. (J) Laminin only view of scans in (H). (K) Representative segmented laminin+ BM of uninjured myofibers or residual BM of injured myofibers.

(L) Cell diameter of GFP+ mononuclear myogenic cells via FACS of TA (n = 2–5 mice/DPI).

(M) Cell volume determined using Fluorender on whole-mount images of EDL (n = 3–7 mice/DPI; n = 14–40 SCs/DPI).

(N–Q) (N) Summed length of all cellular projections/cell, (O) average individual projection length, (P) distribution of SCs with 1–4 projections, and (Q) distribution of SCs with 1–6+ terminal ends of GFP+ SCs in uninjured or Galert (n = 7 mice/DPI; n = 36–42 cells/DPI). Representative SC with two projections (white arrows) and 5 terminal ends (yellow arrows).

(R) Experimental design for labeling proliferative SCs.

(S–U) Whole-mount images of EdU+ GFP+ SCs at 1, 1.5, and 2 DPI (S), quantification of EdU+ GFP+ SCs (T), and representative GFP+ dividing SCs (U) (n = 3–4 mice/DPI; n = 547–2,664 GFP+ SCs/DPI).

(V–Y) Division angles of EdU+ GFP+ SCs 1–2 DPI. (V) Model of possible SC division angles; cell (a) represents planar division, cell (b) represents apical-basal division, and cell (c) represents typical cell observed *in vivo*. (W–Y) Quantification of SC division angles. Red dotted line indicates minimum X-Z division angle for designation of apical-basal division[43] (n = 3–4 mice/DPI and 8–49 EDU+GFP+ SCs measured/DPI). (B-E), (L-O) error bars = SEM. *, **, ***, *** indicate $p < 0.05$, $p < 0.01$, $p < 0.001$, and $p < 0.0001$, respectively. Scale bars, 50 μm.

(legend on next page)

Developmental Cell
Article

CellPress
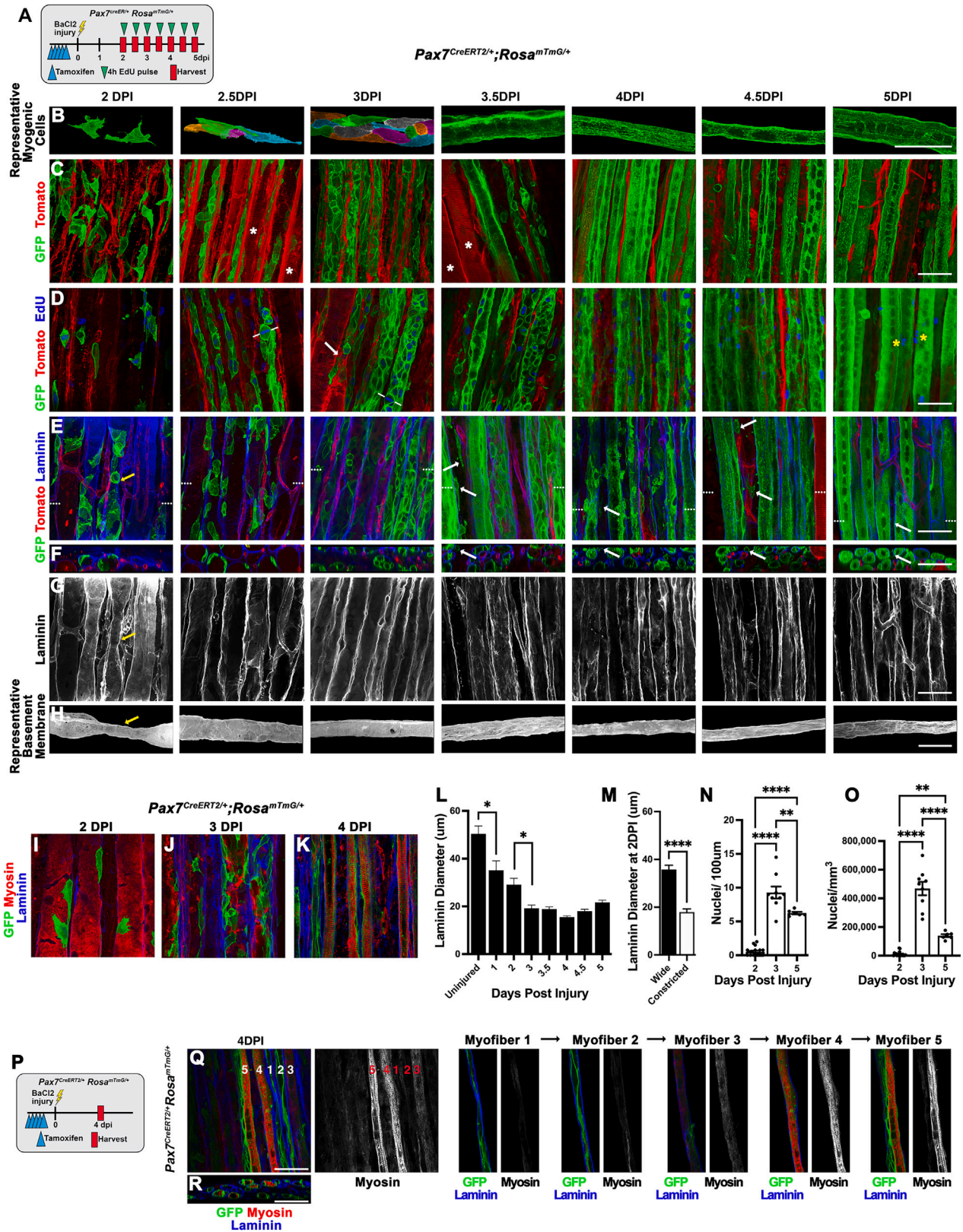
that GFP+ quiescent SCs resided between the sarcolemma and the BM (shown via laminin immunofluorescence), often in close proximity to capillaries (white arrows in Figures 1G–1I; Video S1; see also Verma et al.[41] and Christov et al.[49]). SCs were small (Figures 1L and 1M) and elongated, generally parallel to the long axis of the myofiber (Figures 1G and 1H). Strikingly, individual SCs possessed long cellular projections that branched into numerous terminal ends (Figures 1N–1Q). Although quiescent satellite cells have generally been depicted as fusiform cells with little cytoplasm,[14,50,51] an electron microscopy study[52] and recent *in vivo* studies[41,43,53–55] describe such projections. Our findings demonstrate that our imaging and visualization techniques are sensitive enough to preserve these delicate structures and also provide further evidence that *in vivo* quiescent SCs have a distinctive morphology, with multiple long projections.

SCs have been identified that are neither fully quiescent nor activated, but rather primed for rapid activation, in a state termed Galert.[56] We examined Galert SCs (as defined by Rodgers et al.[56]) to test whether cellular morphology was changed. Previous studies[56] reported that Galert SCs are larger than quiescent SCs. However, we found by FACS Galert SCs were significantly smaller in diameter than quiescent SCs (Figure 1L), although no difference in volume was detected when measured via Fluorender analysis of confocal images (Figure 1M). The number of projections or terminal ends in Galert SCs did not differ (Figures 1N–1Q), but their cellular projections were shorter (Figures 1N and 1O; and similar to findings of Kann et al.[54] and Ma et al.[55]) and is consistent with their being primed for activation.

Upon activation, SCs displayed a greatly altered morphology by 1 DPI. SCs were larger, reaching maximal size by 1.5 DPI (Figures 1L and 1M). The distinctive thin projections of quiescent SCs were absent and instead activated, proliferating SCs (Figures 1R–1T) had broader lamellipodia (Figures 1F–1H), potentially indicative of motile cells.[43,57] Notably, all activated SCs were confined to the inside of residual BM tubes (termed "ghost fibers" by Webster et al.[43]), although the TOM+ sarcolemma and sarcomeres of the injured myofibers were now degraded and largely absent (Figures 1G–1I). Activated SCs continued to generally be close to capillaries (white arrows, Figures 1G–1I).

SCs proliferate via planar divisions

After activation, SCs proliferate to provide myoblasts and myocytes necessary to regenerate myofibers and also to self-renew quiescent SCs. As noted by others,[56,58] the initial round of cell division *in vivo* occurs approximately 30 h after acute injury, while subsequent divisions occur every 8–10 h. Consistent with this, the number of GFP+ myogenic cells expanded 2–3 DPI (Figures 1C–1E). Of considerable interest is whether the early cell divisions are asymmetric (i.e., a SC gives rise to one SC and one committed myoblast) or symmetric (i.e., a SC gives rise to two SCs or to two myoblasts).[12] The niche within which quiescent SCs reside is inherently asymmetric, with the BM establishing the basal surface and the sarcolemma providing the apical surface.[5,12,45] Several studies[11,59,60] based on cultured myofibers with attached SCs have suggested that early asymmetric divisions are manifested as apical-basal cell division events, with the daughter cell adjacent to the BM becoming a quiescent SC, while the daughter adjacent to the sarcolemma differentiates into a MyoD+ myoblast. However, it is unclear whether these *in vitro* observations occur *in vivo*. To test for the frequency of apical-basal divisions *in vivo*, we injected mice with a pulse of EdU (5-ethynyl-2'-deoxyuridine) 4 h prior to harvest (Figure 1R) and analyzed the division angles of EdU+ GFP+ myogenic cells captured in the process of division (identified as pairs of EdU+ SCs, which share an intensely GFP+ membrane, are condensed in shape, and with nuclei closer than 20 um) at 1, 1.5, and 2 DPI (arrows, Figure 1S). At all time points, we found no apical-basal divisions (n = 0/89), but rather planar cell divisions with the two daughter cells aligned parallel to the long axis of the damaged myofiber (Figures 1U–1Y). Thus, although we may have missed rare apical-basal divisions, our data indicates that *in vivo* apical-basal divisions are not widespread and therefore an unlikely mechanism for generating asymmetric cell fates in the first 2 DPI.

Myogenic cells proliferate and accumulate randomly within narrowing residual BM tubes 2–3 DPI

At 2 DPI, GFP+ myogenic cells become flattened and reside adjacent to the inner side of the BM (Figures 2A–2H; Video S2). This flattened morphology is dictated by the presence of residual

Figure 2. Regenerated myofibers form via a wave of density-dependent fusion 3.5–4.5 DPI followed by alignment of myonuclei by 5 DPI

(A) Experimental design for labeling of SCs and their derivatives and whole-mount images (B–H) of EDLs 2–5 DPI (n ≥ 3 mice/DPI).

(B) Representative segmented GFP+ myogenic cells or nascent myofibers. Individual cells pseudo-colored 2.5–3.0 DPI.

(C) Superficial view of GFP+ myogenic cells regenerating myofibers, TOM+ uninjured myofibers with intact sarcomeres (white asterisks at 2.5 and 3.5 DPI), and TOM+ capillaries.

(D) EdU labeling 4 h prior to harvest. At 2.5 and 3 DPI, white lines show division angle of dividing myogenic cells. At 3 DPI, white arrow shows damaged TOM+ myofiber being repaired by GFP+ myogenic cells. At 5 DPI, only peripheral myonuclei are EdU+ (yellow asterisks).

(E–F) Laminin outlines residual BM tubes and surrounds capillaries. Dotted white lines indicate level of cross-sections shown in (F). White arrows in (E) and (F) mark interstitial GFP myogenic cells residing outside BM tubes.

(G) Laminin only of scans in (E).

(H) Representative laminin+ BM tubes. Yellow arrows in (E), (G), and (H) show a necked BM tube.

(I) At 2 DPI, GFP+ myogenic cells are confined to BM tubes where degrading myosin is absent.

(J) At 3 DPI, GFP+ myogenic cells expand around degrading myosin of damaged myofibers within BM tubes.

(K) At 4 DPI, sarcomeric myosin forms within GFP+ regenerated myofibers.

(L) Diameter of laminin+ BM tubes of uninjured and injured myofibers 1–5 DPI (n = 2–3 mice/DPI; n = 4–6 laminin+ tubes/DPI; n = 5 measurements/tube).

(M) Comparison of wide and narrow diameters of necked laminin+ BM tubes at 2 DPI (n = 3 mice; n = 11 tubes).

(N and O) Number of myonuclei per 100 μm length (N) or volume (O) of regenerating myofiber (n = 3 mice/DPI; 3–8 myofibers/DPI).

(P–R) Nascent GFP+ myofibers (experimental scheme, P) immunolabeled with myosin show formation of centralized chains is coincident with formation of organized sarcomeric myosin; representative progression from newly formed myofiber (1) to most mature myofiber (5). (L-O) error bars = SEM. *, **, *** indicate $p < 0.05$, $p < 0.01$, and $p < 0.0001$, respectively. All images' scale bars, 50 μm.

(legend on next page)

Developmental Cell
Article

CellPress
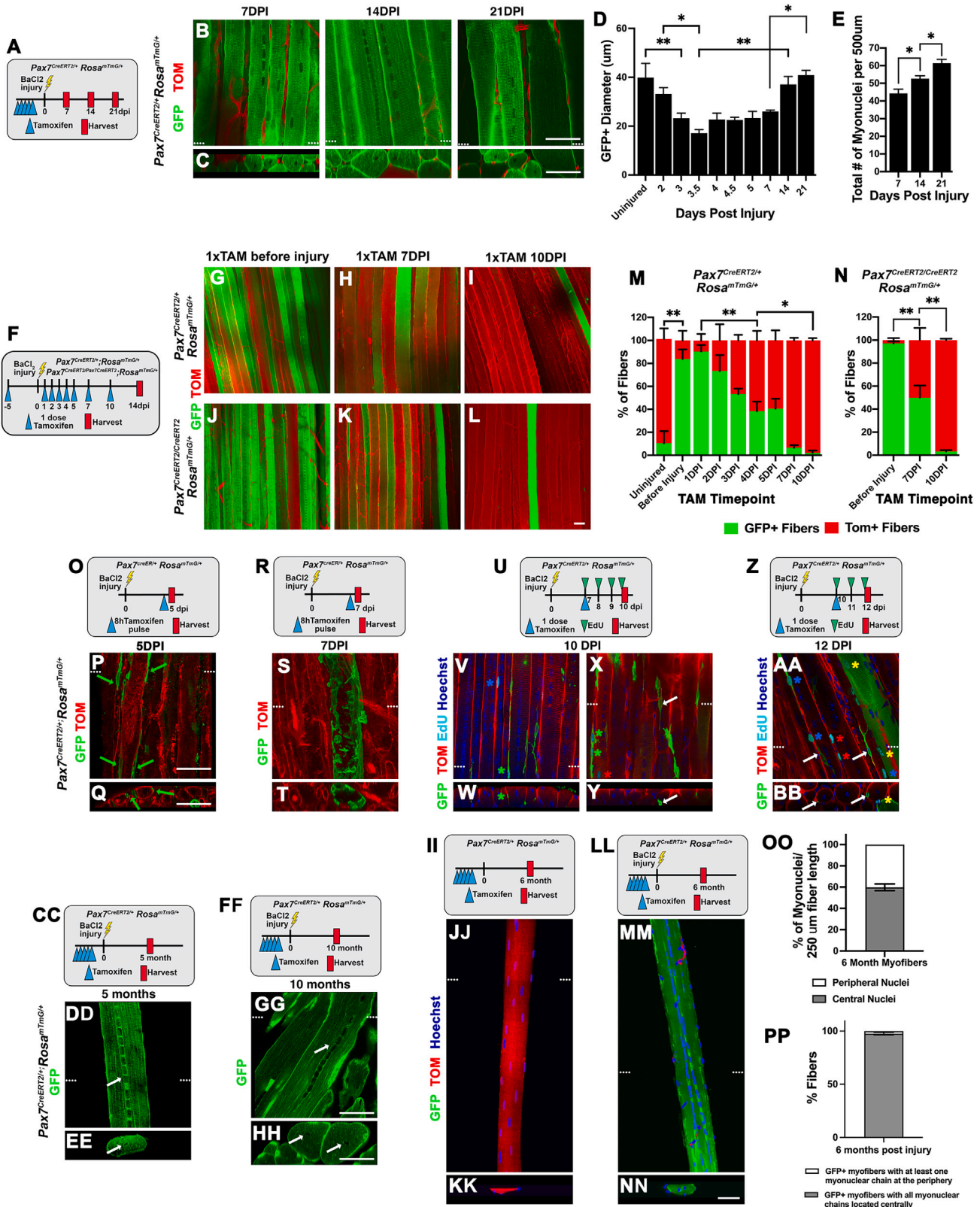
sarcomeric proteins, which fill the interior space of BM tubes (Figure 2I). Myogenic cells became less flattened and more compact and are no longer restricted to the tube periphery 2.5–3 DPI (Figures 2B–2F), as sarcomeric debris is removed (Figure 2J) and eventually replaced by newly formed sarcomeres (Figure 2K).

2–3 DPI myogenic cells are highly proliferative (Figure 2D; quantified in Figure 1T). Previous reports[34,61] hypothesized that the chains of aligned, centralized myonuclei characteristic of regenerated myofibers result from aligned successive planar divisions of myogenic cells. Although we found that early cell divisions are predominantly planar (Figures 1W–1Y), to our surprise we found that GFP+ myogenic cells were randomly distributed within the BM tubes at this stage (Figures 2C–2E; Video S2). This disproves the hypothesis that centralized chains are a simple consequence of successive planar divisions and indicates that such chains must arise from another mechanism.

These images also provide other insights. First, we found that all myogenic cells were sequestered within the BM tubes 0–3 DPI and only appear outside BM tubes beginning at 3.5 DPI (white arrows, Figures 2E and 2F; Video S2). This indicates that initially SCs do not travel outside their associated BM, and therefore regeneration of damaged myofibers is begun by the SCs associated with them. Second, with a robust $BaCl_2$ injury, most regenerating myofibers were composed entirely of GFP+ myogenic cells (indicative of myofibers regenerating *de novo* from SCs), but we also observed hybrid myofibers composed of original TOM+ myofiber stumps flanked by EdU+ GFP+ proliferating myoblasts (white arrow, Figure 2D; Video S2). Thus, integration of old, damaged, and *de novo* myofibers occurs.

During this time, the residual BM tubes underwent significant morphological changes (Figures 2G and 2H; Video S2). In uninjured myofibers, the tubes averaged 50 μm in diameter (Figures 1J and 1K; quantified in Figure 2L) but shrank to 20 μm by 3 DPI (Figures 2G and 2H; quantified in Figure 2L). Particularly at 2 DPI, "necked" tubes with wide and constricted regions were visible (yellow arrows, Figures 2E, 2G, and 2H; quantified in Figure 2M; Video S2)—snapshots of tubes caught in the contraction process. We hypothesize that this contraction results from the clearance of sarcomeric debris (Figures 2I and 2J), such that constricted regions are cleared of debris while wide regions still retain debris.

Density-dependent myocyte-myocyte fusion reestablishes myofibers 3.5–4.5 DPI with chains of centralized nuclei subsequently appearing as sarcomeres form

Between 3.5 and 4.5 DPI, regeneration takes a dramatic turn as a wave of fusion reestablishes most myofibers by 5 DPI (Figures 2C–2F; Video S2). GFP+ myogenic cells rapidly increased (Figure 2C; quantified in Figures 1C and 1D), while the BM tubes shrank to their smallest diameter (Figures 2G and 2H; quantified in Figure 2L). As a consequence of this rapid increase in myogenic cells, and decrease in volume of the tubes in which they reside, myogenic cells reached their maximal density at 3–4 DPI (Figures 2N and 2O). An increase of myogenic cell density to 500,000 cells/mm^3 (Figure 2O) appears to trigger a massive wave of density-dependent fusion. Because fusion occurs nearly synchronously along the length of the regenerating myofibers, myocyte-myocyte fusions likely dominate this process.

By 5 DPI, all regenerated myofibers contain centralized chains of regularly spaced compact nuclei. However, this is not a feature of newly regenerating myofibers at 4–4.5 DPI (Figures 2C–2E; Video S2). Tile scans of whole EDLs at 4.5 DPI (Figures S2A and S2B) showed the ubiquitous presence of newly fused, thin multinucleate myofibers, but chains of regularly spaced compact myonuclei were present only in some regions of these myofibers (asterisks in Figure S2B). This indicates that nuclear chains form secondarily to fusion. We first hypothesized that the centralized chains may form in response to reinnervation of the myofibers. To test this, we transected and retracted the common peroneal nerve to prevent reinnervation and also injured the EDL with $BaCl_2$ (Figure S2C). Denervation was successful, as the EDL mass decreased (Figure S2D). However, centralized chains of regularly spaced nuclei were still apparent at 7 DPI (Figure S2E), demonstrating that innervation is not required for their formation. Instead, we found that central chains of regularly spaced nuclei arose coincident with the periodic banding in GFP+ myofiber membranes that is indicative of sarcomere formation (Figures 2C–2F at 5 DPI; Figure 2K), suggesting that the two processes are linked. Detailed comparison of myofibril and sarcomere formation and myonuclei showed that chains of nuclei only appeared in newly regenerated myofibers that have myofibrils with sarcomeric banding (Figures 2P–2R; Video S2). These observations suggest that the myonuclei are corralled into

---

Figure 3. Myofibers enlarge by addition of peripheral nuclei, with centralized chains generated by 5 DPI persisting for months after regeneration

(A) Experimental scheme for labeling SC-regenerated myofibers 7–21 DPI.

(B and C) Whole-mount images of EDLs 7, 14, and 21 DPI (n ≥ 3 mice/DPI).

(D) Diameter of uninjured and GFP+ regenerated myofibers (n = 3–6 mice/DPI; n = 73–304 GFP+ myofibers/DPI; n = 3 measurements/myofiber).

(E) Myonuclei/500 μm length (n = 3 mice/DPI; n = 18 myofibers/DPI).

(F-N) Experimental scheme (F), whole-mount images of EDLs from *Pax7$^{CreERT2/+}$;Rosa$^{mTmG/+}$* or *Pax7$^{CreERT2/CreERT2}$;Rosa$^{mTmG/+}$* mice (G–L), and quantification (M and N) of SC contribution when labeled at different DPI and assayed at 14 DPI (n = 2–5 mice/DPI; n = 50–214 myofibers/DPI).

(O–T) GFP+ SCs contribute and fuse peripherally to nascent myofibers at 5 (green arrows, P and Q) and 7 DPI (S and T).

(U–BB) SCs at 10 DPI contributing (green asterisks, V and X) or at 12 DPI contributed (yellow asterisks, AA and BB) peripheral EdU+ GFP+ myonuclei. A few EdU+ GFP- myonuclei (red asterisk, X and AA), EdU+ non-myogenic nuclei (blue asterisks, V and AA), and SCs with quiescent morphology (white arrows, X, Y, AA, and BB) are present.

(CC–HH) Chains of centralized myonuclei (white arrows, DD, EE, GG, and HH) persist in regenerated myofibers 5- and 10-months post-injury.

(II–PP) Myofibers from EDLs 6 months post TAM ± injury. TOM+ uninjured myofibers show only peripheral nuclei (II–KK). In GFP+ regenerated myofibers (LL–NN) 60% of myonuclei are centrally located (OO; n = 5 mice and n = 5 myofibers/mouse) and 98% of chains of myonuclei are surrounded by cytoplasm and centrally located (PP; n = 5 mice and n = 48–70 myofibers/mouse). (D-E), (M-N), (OO-PP) error bars = SEM. * and ** indicate *p* < 0.05 and *p* < 0.01. Dotted white lines in (B), (P), (S), (V), (X), (AA), (DD), (GG), (JJ), and (MM) show level of cross-section in (C), (Q), (T), (W), (Y), (BB), (EE), (HH), (KK), and (NN). Images (B–NN), scale bars, 50 μm.

centralized chains of regularly spaced compact nuclei by the formation of the myofibrils in which they are embedded.

Myofibers enlarge by myocyte-myofiber fusion and addition of peripheral myonuclei

Myofibers are regenerated by 5 DPI, but are initially small and enlarge 5–14 DPI (Figures 3A–3D; Video S3). This enlargement is accompanied by an increase in the number of myonuclei through to at least 21 DPI (Figure 3E) and indicates that SCs continue to contribute to nascent myofibers after the initial wave of fusion. To test this, we gave $Pax7^{CreERT2/+};Rosa^{mTmG/+}$ mice a single dose of TAM at various DPI, harvested muscles at 14 DPI, and quantified numbers of GFP+ and TOM+ regenerated myofibers with centralized nuclei (Figures 3F–3I and 3M). As a control, we gave some mice a single TAM dose and harvested uninjured EDLs after 14 days. As expected, a few uninjured myofibers were GFP+, indicating that SCs contributed to these homeostatic myofibers (Figure 3M; see also Pawlikowski et al.[62]). As another control, we gave mice a single TAM dose prior to injury and harvested EDLs at 14 DPI (Figure 3G). This resulted in 84% of regenerated myofibers being GFP+ (Figure 3M) as compared with nearly 100% GFP+ regenerated myofibers when 5 TAM doses were given prior to injury. When one dose of TAM was given at 1 DPI, nearly all regenerated myofibers were GFP+ (Figures 3H and 3M). Single TAM doses given at later days post injury resulted in progressively fewer GFP+ regenerated myofibers (Figures 3I and 3M). Surprisingly, few regenerated myofibers were GFP+ when TAM was delivered at 7 DPI. We reasoned that the efficiency of the $Pax7^{CreERT2/+}$ allele was lower with only a single TAM dose and so repeated the single-dose TAM experiments at 7 and 10 DPI experiments with $Pax7^{CreERT2/CreERT2};Rosa^{mTmG/+}$ mice (Figures 3J–3L and 3N). With two Cre copies, 50% of regenerated myofibers were GFP+ when TAM was delivered at 7 DPI (Figures 3K and 3N). Even with two Cre copies, few regenerated myofibers were GFP+ when TAM was delivered at 10 DPI (Figures 3L and 3N), indicating that few SCs detectably contributed to regeneration of myofibers at this time point, even though the number of myonuclei slowly increased until at least 21 DPI (Figure 3E). Overall, these data indicate that the major phase of SC contribution to regeneration of myofibers is complete by 10 DPI.

Given that centralized chains of myonuclei are present by 5 DPI, we next tested the location of myonuclei contributed by SCs at 5 and 7 DPI by giving $Pax7^{CreERT2/+};Rosa^{mTmG/+}$ mice a single dose of TAM 8 h prior to harvest (Figures 3O–3T). The majority of regenerated myofibers were TOM+, as they were generated by SCs prior to TAM. Elongate GFP+ myogenic cells (but without the thin projections distinctive of quiescent SCs) were found fusing peripherally to regenerating TOM+ myofibers at 5 DPI (green arrows, Figures 3P and 3Q; Video S3). At 7 DPI, we captured GFP+ myogenic cells fusing to form a peripheral scaffold around a regenerated myofiber (Figures 3S and 3T; Video S3). These data indicate that SCs fusing to regenerating myofibers after 4 DPI contribute peripheral myonuclei. In addition, delivery of EdU 4 h prior to 5 DPI harvest labeled only peripheral myonuclei (yellow asterisks, Figure 2D; Video S2). Furthermore, EdU administration later than 5 DPI (at 10 or 12 DPI; Figures 3U–3BB; Video S3) labeled only recently adding (green asterisks, Figures 3V–3X; Video S3) or added peripheral myonuclei (yellow asterisks, Figures 3AA and

3BB). Thus, after formation of centralized chains by 4.5 DPI, all subsequently added myonuclei are peripheral.

SCs with quiescent morphology appear by 10 DPI

There has been considerable debate about when SCs return to quiescence and repopulate their niche between the myofiber's BM and sarcolemma.[11,59,60,63–65] We found that quiescent SCs are morphologically unique, typically with 2 thin projections (Figures 1F–1H and 1N–1Q). Our experiments labeling all SCs and their derivatives via TAM prior to injury did not allow us to readily identify the re-appearance of quiescent SCs because of the high density of GFP+ myogenic cells. Instead, we identified morphologically distinct quiescent SCs by a single dose of TAM prior to harvest (8 h prior to harvest at 5 or 7 DPI or 48 h prior to harvest at 10 or 12 DPI). We readily found morphologically quiescent SCs that were EdU− (see EdU labeling strategies in Figures 3U and 3Z) at 10 and 12 DPI (white arrows, Figures 3X–3BB; Video S3). However, we did not identify morphologically distinctive quiescent SCs at 5 or 7 DPI. Although we cannot exclude that molecularly distinct quiescent SCs are present earlier, our data indicate that morphologically distinct quiescent SCs appear after 7 DPI.

Centralized chains of myonuclei persist in regenerated myofibers for months

Although centralized chains of myonuclei have long been recognized as a hallmark of regenerating myofibers,[32–35] it has been unclear how persistent these chains are. In development[66] and in culture,[67] centralized myonuclei transition to peripheral nuclei. Therefore, it has been assumed by many[36,37] that the chains of centralized myonuclei eventually migrate peripherally. However, a more recent study[33] indicates that centralized nuclei persist for nearly 2 years, although this study was limited by the lack of a method to establish which individual myofibers were regenerated independent of the presence of centralized nuclei. Our genetic labeling of SCs and their derivatives now allows us to tag regenerated myofibers and determine the fate of the centralized chains of myonuclei. We gave TAM to $Pax7^{CreERT2/+};Rosa^{mTmG/+}$ mice, injured EDLs, and harvested EDLs 5- or 10-months post injury (Figures 3CC–3HH). As expected, most myofibers were GFP+, indicating that they were regenerated. Strikingly, we found that nearly every GFP+ regenerated myofiber contained regions with centralized chains of myonuclei (Figures 3CC–3HH; n = 47/48 myofibers in 2 mice). To further detail the location and prevalence of centralized chains, we harvested another cohort of mice at 6 months post injury, isolated myofibers, and analyzed and quantified the three-dimensional location of Hoechst+ myonuclei on the confocal (Figures 3II–3NN). We found that 100% of regenerated myofibers had centralized nuclei (n = 288/288) and 60% of myonuclei in the myofibers were centrally located, almost always in chains (Figure 3OO). In 98% of the myofibers (n = 281/288, Figure 3PP) the chains of myonuclei (distinctive of regenerated myofibers) were centrally located, with only 7 myofibers with 1 chain of myonuclei peripherally located. Thus, we conclude that the overwhelming majority of centralized nuclei formed during regeneration do not migrate to the periphery and indelibly mark regenerated myofibers, at least until 10 months.
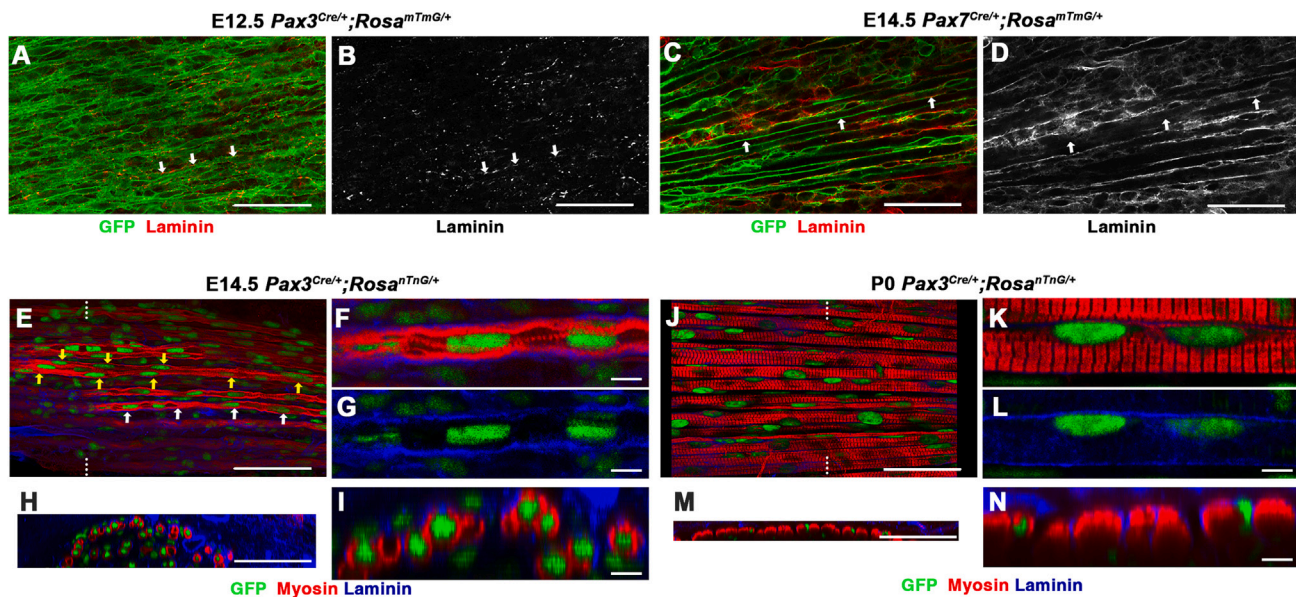
Figure 4. Development of myofibers is distinct from regeneration; myogenesis begins in the absence of continuous BMs and myonuclei begin centralized and move peripherally

(A and B) TA at E12.5 of $Pax3^{Cre/+};Rosa^{mTmG/+}$ mice showing GFP+ forming myofibers with speckly laminin (white arrows).

(C and D) TA at E14.5 of $Pax7^{Cre/+};Rosa^{mTmG/+}$ mice showing areas of continuous laminin adjacent to GFP+ sarcolemma (white arrows show one myofiber with no laminin on left side, but laminin on right side).

(E–N) $Pax3^{Cre/+};Rosa^{nTnG/+}$ mice at E14.5 (E–I) or P0 (J–N) showing primary myofibers with single row of centralized nuclei (white arrows, E) or secondary myofibers with several rows of nuclei (yellow arrows, E). Myonuclei are peripheral by P0 (J–N). (H) and (M) are cross-sections of (E) and (J), respectively; location of cross-sections shown as white lines on (E) and (J). (F), (G), (I), (K), (L), and (N) are magnifications of (E), (H), (J), and (M), respectively. (A–E), (H), (J), and (M) scale bars, 50 μm; (F), (G), (I), (K), (L), and (N) scale bars, 5 μm.

Regeneration differs from the development of myofibers

Muscle development and regeneration are often suggested to use similar molecular and cellular processes.[39,40] However, development and regeneration have different temporal and functional constraints. In mice, limb myogenesis occurs from E10.5 to E18.5 *in utero* in the absence of functional demands on developing muscle.[39,68,69] In contrast to development, we find that myofibers are rapidly regenerated within 4.5 DPI—presumably necessitated by the functional requirements of an ambulatory mouse. The difference in timing and functional constraints suggests that muscle development and regeneration differ, and therefore we generated whole-mount *in vivo* images of developmental myogenesis to compare with our images of regeneration.

We examined the TA at E12.5, when embryonic myogenic cells fuse to make primary myofibers, and at E14.5, when fetal myogenic cells fuse to primary myofibers and fuse to one another to make secondary myofibers.[68,69] We first examined whether the BM was essential for myofiber development. We used E12.5 $Pax3^{Cre/+};Rosa^{mTmG/+}$ embryos in which $Pax3^{Cre}$ genetically labels limb embryonic muscle progenitors and their derivatives.[69] At this stage, myogenic cells fuse to make myofibers with continuous GFP+ membranes (white arrows, Figure 4A; Video S4). However, in contrast to regeneration, this fusion happens in the absence of a continuous laminin+ BM, with BM appearing as small dots adjacent to newly forming myofibers (white arrows, Figures 4A and 4B; Video S4). We also examined E14.5 $Pax7^{Cre/+};Rosa^{mTmG/+}$ embryos in which $Pax7$-Cre labels fetal limb muscle progenitors and their derivatives.[69]

TA myofibers were larger in diameter (white arrows, Figure 4C; Video S4) than at E12.5, and parts of the myofibers have areas of continuous laminin+ BM (white arrows, Figures 4C and 4D; Video S4). Thus, unlike regeneration, a continuous BM is absent during primary myogenesis but, as development proceeds, a BM builds up to surround all myofibers during fetal myogenesis.

We also investigated the location of myonuclei in the developing myofibers, as it has been proposed that nascent myofibers have centralized nuclei that move peripherally as myofibers mature,[37,38] although this model is largely based on *in vitro* studies. We examined E14.5 $Pax3^{Cre/+};Rosa^{nTnG/+}$ embryos in which all myogenic nuclei are GFP+, which were also labeled with laminin and perinatal myosin antibodies (Figures 4E–4I; Video S4). At this stage, there were primary myofibers with a single row of dispersed myonuclei located centrally and surrounded on most sides by irregular, partially formed myofibrils (white arrows, Figures 4E and 4F–4I). There were also secondary myofibers (yellow arrows, Figure 4E), which contained more than one row of myonuclei, and the additional nuclei were peripherally located—likely the result of recently fused myocytes. Notably, E14.5 myonuclei differ from the centralized myonuclei of regenerated myofibers, which form centralized chains of regularly spaced, compact myonuclei. At P0, TA myofibers were larger, myofibrils aligned in distinct sarcomeres, and, importantly, all myonuclei were located peripherally—outside the myofibrils and beneath the BM (Figures 4J–4N; Video S4). Therefore, unlike regeneration, as developing myofibers grow in diameter, their myonuclei shift to a peripheral position.

(legend on next page)

Developmental Cell
Article

CellPress
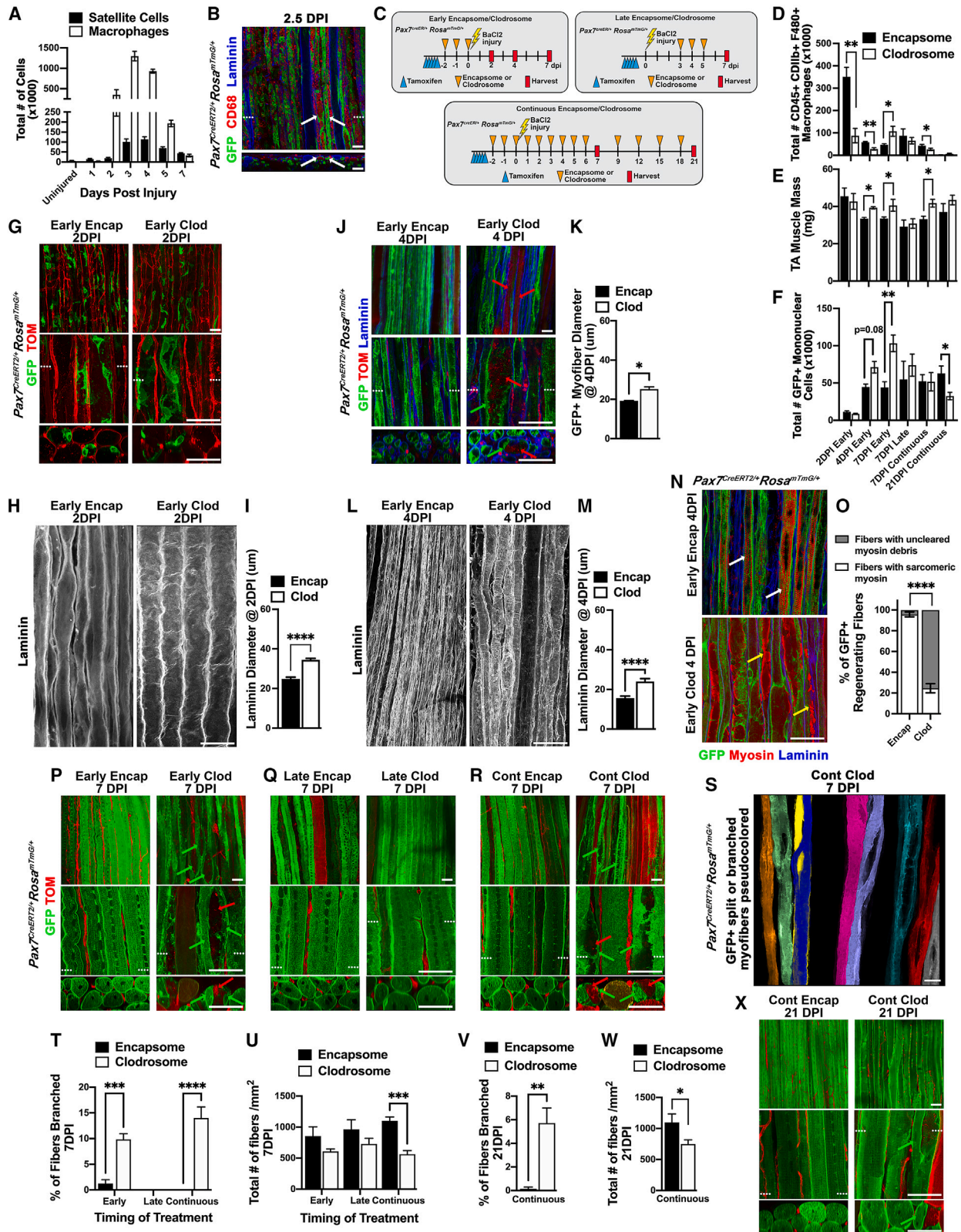
Macrophages are required for proper density-dependent fusion of myogenic cells

Fusion of myogenic cells at 3.5–4.5 DPI rapidly reestablishes myofibers, and our data suggest that this event is density-dependent. This increase in myogenic cell density is a consequence of increasing numbers of myogenic cells contained within a shrinking BM, which reaches a minimal size during this critical time. We hypothesized that this BM shrinkage is due to the removal of myofibril debris within the BM tubes by macrophages, which have a critical role in clearing cellular debris (efferocytosis).[70–73]

To test whether macrophages are critical for BM shrinkage, we experimentally depleted macrophages during regeneration. First, we documented that macrophages were recruited to muscle, reached peak numbers at 3 DPI (Figures 5A and S1), and migrated inside the BM tubes in close contact with myogenic cells (white arrows, Figure 5B; Video S5). Then, we depleted macrophages at different time points via intraperitoneal delivery of clodrosome, a liposome-encapsulated clodronate, which depletes phagocytic peripheral monocytes and macrophages infiltrating into muscle (Figure 5C;[74–76]). Delivery of encapsome, liposomes lacking clodronate, served as a negative control.

Delivery of clodrosome prior to injury (Figure 5C) resulted in a substantial depletion of macrophages in the muscle by 2 DPI (Figure 5D; similar to Summan et al.[75] and Kawanishi et al.[77]). Macrophage depletion did not result in any change in muscle mass, number of GFP+ mononuclear cells, or cellular signs of SC activation at 2 DPI (Figures 5E–5G). However, at 2 DPI, the diameter of BM tubes remained wider with macrophage depletion (Figures 5H and 5I). At 4 DPI, muscles in which clodrosome was delivered prior to injury had a significant reduction in macrophages (Figure 5D) and were heavier (Figure 5E). In control muscles, most myofibers were reestablished by the wave of density-dependent fusion (Figures 5J and S3; Video S5). In contrast, clodrosome treatment resulted in wider GFP+ myofibers (Figures 5J and 5K) and wider BM tubes (Figures 5L and 5M). Within these wider myofibers were fragments of residual, un-phagocytized TOM+ sarcolemma from the damaged myofibers (red arrows, Figure 5J). Although newly formed sarcomeres were present in nascent myofibers in control muscles (white arrows, Figures 5N, 5O, and S3; Video S5), myofibers with residual disorganized myosin debris were common in clodrosome-treated muscles (yellow arrows, Figures 5N, 5O, and S3; Video S5). This physical impedance of un-phagocytosed sarcomeric proteins and cell membranes led to aberrant fusion of myogenic cells, resulting in regenerated myofibers with wide gaps (green arrows, Figures 5J and S3; Video S5). Consistent with this, the number of mononuclear, unfused GFP+ myogenic cells was somewhat elevated (p = 0.08, Figure 5F).

Overall, these experiments demonstrate that phagocytosis by macrophages is critical for clearance of necrotic debris, allowing BM tubes to contract and density-dependent fusion to proceed unimpeded.

Depletion of pro-inflammatory macrophages during regeneration leads to split and branched myofibers

To see whether macrophage depletion had later effects on muscle regeneration, we analyzed muscles at 7 DPI. Clodrosome treatment prior to injury caused 10% of regenerated myofibers to have an aberrant morphology; myofibers were split or branched (green arrows, Figure 5P; quantified, Figure 5T), with some retaining uncleared TOM+ debris (red arrows, Figure 5P). We also tested whether continuous delivery of clodrosome would exacerbate the phenotype (Figure 5C). We found that 14% of regenerated myofibers were branched (green arrows, Figures 5R and 5S; Video S5; quantified, Figure 5T), often surrounding residual debris (red arrows, Figure 5R), but there was no statistical difference in the number of branched myofibers between early and continuous clodrosome delivery (Figure 5T). However, continuous clodrosome led to the regeneration of fewer myofibers (Figure 5U). We also attempted to deplete macrophages later during regeneration (3–5 DPI; Figure 5C), but at 7 DPI macrophages were not significantly depleted and the morphology of myofibers was similar to control (Figures 5D, 5Q, 5T, and 5U). Nevertheless, as early clodrosome treatment (causing macrophage depletion at 2 and 4 DPI, but not at 7 DPI) and continuous treatment (causing macrophage depletion through 7 DPI) had a similar branching phenotype (Figures 5D and 5T), this suggests that early macrophages, which are pro-inflammatory macrophages,[70] are the cause of this phenotype.

We also tested whether macrophage depletion caused a persistent phenotype at 21 DPI. With continuous clodrosome delivery, macrophages were depleted at 7 DPI, although no discernable difference was detected at 21 DPI (when macrophages return to low basal levels) (Figure 5D). Nevertheless,

Figure 5. Macrophages are essential to clear debris, enabling density-dependent myogenic cell fusion and preventing formation of branched myofibers

(A) FACs quantification of macrophages and SCs during regeneration (n = 2–4 mice/DPI).

(B) At 2.5 DPI, CD68+ macrophages penetrated the BM tubes and reside adjacent to GFP+ myogenic cells (white arrows).

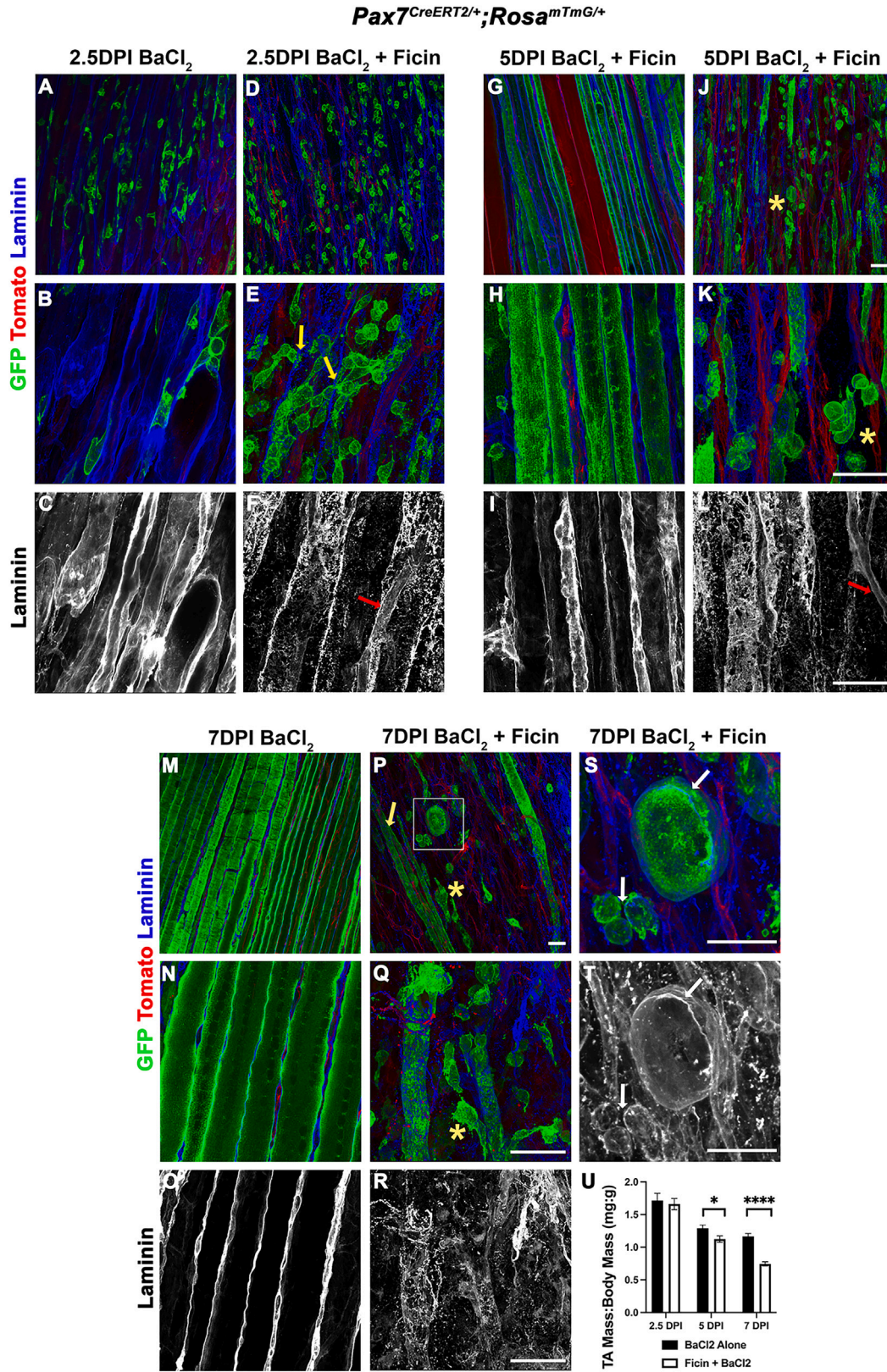(C) Experimental schemes for macrophage depletion.

(D–F) At different DPIs and with early, late, or continuous clodrosome (or control encapsome) administration to TAs, quantification of macrophages via FACS (D), TA mass (E), or GFP+ mononuclear myogenic cells via FACS (F) (n = 2–7 mice/condition).

(G–I) Macrophage depletion does not affect SC activation, but prevents normal BM shrinking (n = 3 mice/condition; n = 51–53 myofibers/condition).

(J–O) At 4 DPI, macrophage depletion leads to poorly fused GFP+ myogenic nascent myofibers (green arrows, J) with persistent TOM+ debris (red arrows, J) that are wider (J and K) (n = 3 mice/condition; 65–83 myofibers/condition), within wider BM tubes (L and M) (n = 3 mice/condition; n = 25–27 myofibers/condition). In controls, most myofibers are GFP+ regenerated fibers with sarcomeric myosin (white arrows, N), while clodrosome treatment results in continued presence of necrotic fibers with disorganized myosin debris (yellow arrows, N) at 4 DPI (N and O, n = 3 mice/condition; 101–114 myofibers/condition).

(P–U) At 7 DPI, early (P) or continuous (R) macrophage depletion causes aberrantly fused and branched myofibers (green arrows) with persistent TOM+ sarcolemma debris (red arrows), but such an effect is not seen with late clodrosome administration (Q). At 7 DPI, branched or split myofibers pseudo-colored in (S) and frequency of branching and loss of myofibers quantified in (T and U) (n = 3–6 mice/condition; 197–655 myofibers/condition).

(V–X) At 21 DPI, continuous clodrosome leads to more branched myofibers and fewer regenerated myofibers (n = 5–6 mice/condition; n = 387–646 myofibers/condition). (D-F), (I), (M), (O), (T-W) error bars = SEM. *,**,***,**** indicate $p < 0.05$, $p < 0.01$, $p < 0.001$, $p < 0.0001$, respectively. Dotted white lines in (G), (J), (P)–(R), and (X) middle panel show level of cross-section in lower panel. Scale bars, 50 μm.

Pax7$^{CreERT2/+}$;Rosa$^{mTmG/+}$

(legend on next page)

Developmental Cell
Article

CellPress

we found that macrophage depletion led to persistent elevated levels of branched myofibers and decreased numbers of regenerated myofibers (Figures 5V–5X).

Residual BM tubes are required for proper muscle regeneration

Our experiments suggest that the residual BM tubes are critical for muscle regeneration. To test the importance of intact BM tubes, we disrupted the BM by treatment with ficin, a serine protease derived from fig trees and previously used to disrupt *in vivo* BM[78] and, in particular, muscle BM.[79] At 2.5 DPI, disruption of the BM altered the morphology of the myogenic cells: instead of the characteristic flattened shape of this stage, myogenic cells were rounded with short, thin protrusions (Figures 6A–6F; Video S6). In addition, myogenic cells were able to exit the tubes (yellow arrows, Figure 6E). The most dramatic effects of BM disruption were seen at 5 and 7 DPI (Figures 6G–6R; Video S6). Instead of regenerated linear myofibers with centralized myonuclei (Figures 6G, 6I, and 6M–6O), myogenic cells fused to make aberrant short or branched myofibers (yellow arrow Figure 6P) or completely dysmorphic muscles (yellow asterisks, Figures 6J, 6K and 6P–6R). Interestingly, these dysmorphic muscles reveal that newly regenerated muscle begins making its own BM by 7 DPI (white arrows, Figures 6S and 6T). The general reduction in regenerated muscle is evidenced in the lower muscle weights after ficin treatment (Figure 6U). Overall, these experiments demonstrate that intact BM tubes are important for initially sequestering activated SCs prior to 3 DPI, promoting the wave of density-dependent fusion to make myofibers, and insuring that myofibers are linear and correctly oriented.

DISCUSSION

By genetically labeling SCs, as well as imaging and reconstructing regeneration in three dimensions, our study has provided surprising insights and leads to a synthetic model of how SCs reestablish muscle structure (summarized in Figure 7).

SCs have two essential roles during regeneration: to regenerate myofibers and replenish themselves. After activation, SCs proliferate by a combination of symmetric and asymmetric divisions,[65] and the decision to differentiate or self-renew involves an asymmetric cell division that leads to asymmetric fates. It has been proposed that early asymmetric, apical-basal divisions lead to early SC replenishment.[11,59,60,63] Yet, our *in vivo* quantification of SC division angles found only planar cell divisions 1–2 DPI and agrees with the results of Webster and colleagues.[43] Together, these data do not support a model whereby early apical-basal divisions are a pervasive mechanism for SC self-renewal. Two recent studies suggest that *in vivo* asymmetric cell division and SC self-renewal occur later in regeneration,

generally at 5 DPI or later.[64,65] Consistent with these studies, we find that morphologically distinct quiescent SCs are not present until after 7 DPI, suggesting that the first priority for SCs is to regenerate myofibers and then, only secondarily, to reestablish a pool of quiescent SCs.

The main insights of our analysis are on regeneration of myofibers and tissue architecture. Unexpectedly we uncovered that SCs and their myogenic derivatives regenerate myofibers via two distinct phases of fusion (Figure 7). First, a massive wave of density-dependent myocyte-myocyte fusion regenerates myofibers 3.5–4.5 DPI. Given that the myogenic cells are initially sequestered within the BM tubes, it is likely that each nascent myofiber is derived from SCs associated with the damaged myofiber they are replacing. Notably, the myonuclei generated during this phase form the characteristic centralized chains of myonuclei. Our experiments pulsing mice with EdU just prior to harvest demonstrate that, after this primary phase of fusion, subsequently fusing myocytes never contribute to these centralized nuclei. Complementary studies with continuous bromodeoxyuridine (BrdU)[34] or EdU[64] labeling during multiple time windows during regeneration confirm that only myogenic cells labeled during 0–4 DPI contribute to centralized nuclei.

After this rapid wave of fusion, a second phase of fusion extends from 5 to 10 DPI. This phase is density-independent and dominated by myocyte-myofiber fusion. These fusion events give rise to the peripheral myonuclei of regenerated myofibers, as found by our experiments labeling cells via pulses of TAM and/or EdU prior to harvest and confirmed by the EdU and BrdU labeling experiments of Wada et al.[34] and Cutler et al.[64] Fusion of myocytes to myofibers is important for increasing the number of myonuclei and diameter of the regenerating myofibers. The appearance of myogenic cells outside the BM tubes beginning at 3.5 DPI suggests that some myocytes may derive from SCs originating from neighboring myofibers. Although grafted SCs can migrate into adjacent myofibers,[80,81] it is currently unclear whether endogenous SCs only regenerate their home myofiber or whether they contribute to the regeneration of other myofibers.[13,14]

Our research also elucidates the etiology of the organization of myonuclei of regenerated myofibers. The distinctive centralized chains of myonuclei arise just after the wave of density-dependent fusion and are strongly correlated with myofibril assembly. Previous studies have linked myofibril formation and myonuclei location,[67,82,83] but *in vitro* studies found that forming myofibrils drive nuclei to the myofiber periphery.[67] However, we find in *de novo* myofibers regenerated *in vivo*, that the initial myonuclei remain in centralized chains; we hypothesize that the rapidity of myocyte-myocyte fusion, nearly synchronous formation of myofibrils, and the enclosing BM traps and positions myonuclei into centralized chains. We also show that these chains remain

Figure 6. Residual BM tubes are critical for constraining SCs, promoting fusion, and aligning regenerating myofibers
(A–F) Enzymatic degradation of the residual BM tubes (D–F) allows activated SCs to exit tubes (yellow arrows in E) as compared with control injury (A–C) in which SCs are sequestered in tubes at 2.5 DPI. After ficin treatment, BM is quickly reestablished around capillaries (red arrow).
(G–L) Myogenic cells fuse aberrantly (yellow asterisks) when BM tubes are disrupted (J–L) as compared with linear myofibers formed in the presence of BM tubes (G–I). Red arrow shows capillaries with reestablished BM.
(M–T) Normally at 7 DPI, linear myotubes with central chains have regenerated (M–O). After ficin treatment (P–T), myogenic cells continue to fuse aberrantly, resulting in dysmorphic (yellow asterisks) and branched myofibers (yellow arrow). Dysmorphic muscle begins to form new BM (white arrows, S and T).
(U) Disruption of BM tubes leads to smaller muscles. Error bars = SEM. n = 4–5 mice/time point. Images (A, D, G, J, M, and P); scale bars, 50 μm in (J) and (P). Images (B, C, E, F, H, I, K, L, N, O, Q, and R); scale bars, 50 μm in (K), (L), (Q), and R. Images (S and T), scale bars, 50 μm.

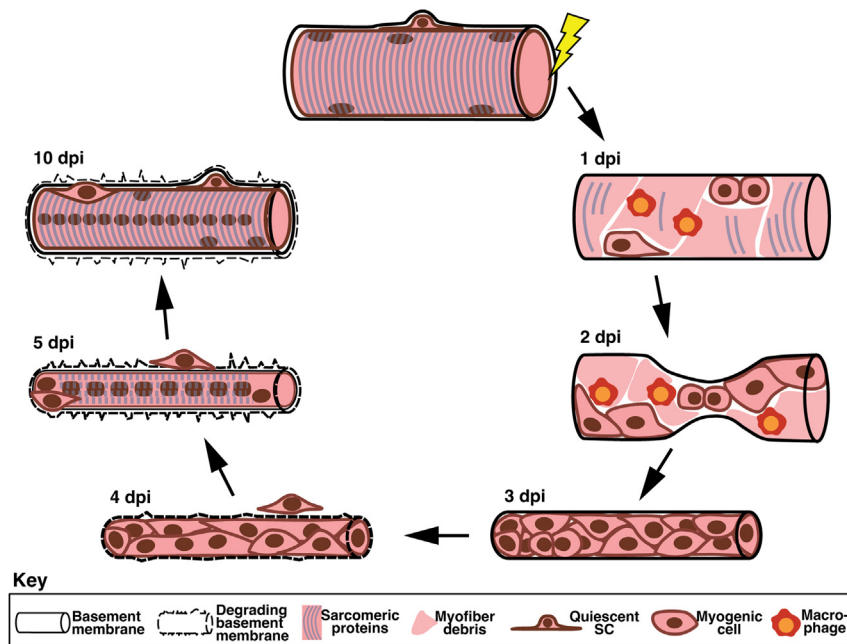## Regeneration after acute injury and myofiber destruction

Figure 7. Model of cellular dynamics of regeneration

1 DPI: within residual BM, degradation of sarcolemma, macrophage entry and clearance of debris, and SC activation and proliferation. 2 DPI: necking and shrinking of BM tube within which macrophages clear debris and myogenic cells proliferate. 3 DPI: BM tube narrows and myogenic cells coalesce into columns. 4 DPI: BM tube narrowest and wave of density-dependent myocyte-myocyte fusion leads to myofibers with unaligned myonuclei. Some myogenic cells are found outside BM tubes. 5 DPI: myofibers reestablished with myonuclei derived from myocyte-myocyte fusion positioned into centralized chains by forming sarcomeres. New BM forming as old one degrades. 10 DPI: myofibers continue to enlarge via occasional myocyte-myofiber fusion events and addition of peripheral myonuclei. Quiescent SCs present in niche.

for at least 10 months after injury, suggesting that they may persist indefinitely and indelibly mark regenerated myofibers. The peripheral myonuclei that are commonly found in regenerated myofibers are not the result of originally centrally located nuclei moving to the myofiber periphery but instead derive from the later myocyte-myofiber fusion events. Thus, the common interpretation that centralized myonuclei mark actively regenerating myofibers needs to be revised.[37,84] An important consequence of this finding is that all *de novo* myofibers regenerated after myofiber destruction will have central myonuclear chains that may compromise mechanical output. Intuitively, centralized myonuclei would seem to disrupt sarcomere function.[37] Regenerated muscle is biomechanically stiffer than uninjured muscle,[85] but whether individual, regenerated myofibers with centralized myonuclei have an altered functional output has not been formally tested.

Our work highlights the importance of the residual BM for multiple aspects of muscle regeneration (Figure 7). During early stages, the BM acts as a selective cell filter; BM tubes retain SCs and their myogenic derivatives, while allowing free penetration of infiltrating macrophages. Such a function had been suggested by older electron micrograph studies,[14,19,86] but could only be demonstrated with our genetic labeling and whole-mount imaging. Importantly, the BM is not significantly degraded by the macrophages, preserves the orientation of the damaged myofibers, and acts as a scaffold to regenerate correctly oriented myofibers. The subsequent constriction of the intact BM (also observed in isolated regenerating human myofibers by Mackey and Kjaer[82]), enabled by macrophage clearance of cellular debris, promotes the rapid fusion and reestablishment of myofibers. As revealed by electron micrography studies,[16,17,82] the residual BM is gradually degraded. Consistent with our findings (Figures 6S and 6T), a new BM appears by 7 DPI and, on normally regenerating myofibers, is nested inside the old one.[16,17,82]

Interestingly, our experiments reveal two different mechanistic causes of split or branched myofibers. Branched myofibers are characteristic of dystrophic muscle,[23,28] arise during regeneration,[28] and are functionally deficient and more prone to damage compared with unbranched myofibers.[87,88] Several processes have been proposed to cause branched myofibers: aberrant fusion of myocytes,[18,23,31,89,90] defects in myogenic cell migration,[91] or fusion of two myofibers.[92] Here, we show two additional means. First, defects in the residual BM (characteristic of multiple dystrophies[93]) can cause branched myofibers, presumably by SCs escaping the normal confines of the BM tubes to migrate and fuse aberrantly. Second, depletion of macrophages also can cause branched myofibers, as cellular debris physically impedes fusion and formation of linear myofibers.

Finally, our research elucidates similarities and differences between limb myogenesis during development and during regeneration. During both, myogenesis occurs in two phases. The first phase (embryonic myogenesis or density-dependent myocyte-myocyte fusion in regeneration) establishes nascent myofibers, while the second phase (fetal myogenesis or myocyte-myofiber fusion in regeneration) enlarges these myofibers. The second phase is similar between development and regeneration; myogenesis proceeds over many days via myocyte-myofiber fusion, resulting in peripheral myonuclei in myofibers surrounded by a BM. However, the first phase differs. In regeneration, rapid density-dependent myocyte-myocyte fusion within a BM tube results in chains of myonuclei locked into a central location. In contrast, embryonic myogenesis occurs in the absence of a BM, extends over days, may not be density-dependent, and results in centrally located myonuclei that which migrate to the myofiber periphery. These findings indicate that the molecular and cellular regulation of fusion[94] and myonuclear positioning[37] likely differ between development and regeneration.

Limitations of the study

Our whole-mount *in vivo* analysis provides significant insights into the three-dimensional processes necessary to regenerate

Developmental Cell
Article

CellPress

muscle after an acute, experimentally induced myofiber-destroying injury in which the BM remains intact and the injury site remains sterile.[14,15,71] However, regeneration occurs in multiple different contexts in which damage and regeneration may occur chronically (e.g., during muscle diseases),[95] tissue architecture is damaged (BM removal during volumetric loss),[96,97] or the macrophage or inflammatory response is altered (e.g., due to disease or infection by viruses tropic to muscle).[71,98,99] Whether the regenerative processes we have identified are conserved in these other contexts awaits future research that employs three-dimensional imaging. Such research will further elucidate the general principles guiding regeneration of skeletal muscle, a tissue with a complex tissue architecture.

STAR★METHODS

Detailed methods are provided in the online version of this paper and include the following:

- KEY RESOURCES TABLE
- RESOURCE AVAILABILITY
  - Lead contact
  - Materials availability
  - Data and code availability
- EXPERIMENTAL MODEL AND STUDY PARTICIPANT DETAILS
  - Mice
- METHOD DETAILS
  - Tamoxifen, EdU, and Encapsome/Clodrosome injections
  - Muscle injury and basement membrane disruption
  - Common peroneal nerve denervation
  - FACS analysis
  - Myofiber preps
  - Muscle clearing for whole-mount imaging of endogenous fluorescence
  - Whole-mount immunostaining
  - Whole-mount imaging and 3D rendering
  - Quantification of myogenic cell and BM morphology
- QUANTIFICATION AND STATISTICAL ANALYSIS

SUPPLEMENTAL INFORMATION

Supplemental information can be found online at https://doi.org/10.1016/j.devcel.2024.03.017.

AUTHOR CONTRIBUTIONS

B.C.C., J.B.S., and G.K. designed experiments; B.C.C., J.B.S., M.M.S., and R.V.M. conducted experiments; B.C.C., J.B.S., M.M.S., R.V.M., and G.K. analyzed data; M.V. provided technical assistance; B.C.C. and G.K., with help from J.B.S., wrote the paper.

REFERENCES

1. Morrison, S.J., and Kimble, J. (2006). Asymmetric and symmetric stem-cell divisions in development and cancer. Nature 441, 1068–1074. https://doi.org/10.1038/nature04956.

2. Dumont, N.A., Bentzinger, C.F., Sincennes, M.C., and Rudnicki, M.A. (2015). Satellite Cells and Skeletal Muscle Regeneration. Compr. Physiol. 5, 1027–1059. https://doi.org/10.1002/cphy.c140068.

3. Relaix, F., and Zammit, P.S. (2012). Satellite cells are essential for skeletal muscle regeneration: the cell on the edge returns centre stage. Development 139, 2845–2856. https://doi.org/10.1242/dev.069088.

4. Hawke, T.J., and Garry, D.J. (2001). Myogenic satellite cells: physiology to molecular biology. J. Appl. Physiol. (1985) 91, 534–551. https://doi.org/10.1152/jappl.2001.91.2.534.

5. Mauro, A. (1961). Satellite cell of skeletal muscle fibers. J. Biophys. Biochem. Cytol. 9, 493–495. https://doi.org/10.1083/jcb.9.2.493.

6. Lepper, C., Partridge, T.A., and Fan, C.M. (2011). An absolute requirement for Pax7-positive satellite cells in acute injury-induced skeletal muscle regeneration. Development 138, 3639–3646. https://doi.org/10.1242/dev.067595.

7. Murphy, M.M., Lawson, J.A., Mathew, S.J., Hutcheson, D.A., and Kardon, G. (2011). Satellite cells, connective tissue fibroblasts and their interactions are crucial for muscle regeneration. Development 138, 3625–3637. https://doi.org/10.1242/dev.064162.

8. Sambasivan, R., Yao, R., Kissenpfennig, A., Van Wittenberghe, L., Paldi, A., Gayraud-Morel, B., Guenou, H., Malissen, B., Tajbakhsh, S., and Galy, A. (2011). Pax7-expressing satellite cells are indispensable for adult skeletal muscle regeneration. Development 138, 3647–3656. https://doi.org/10.1242/dev.067587.

9. Yurchenco, P.D. (2011). Basement membranes: cell scaffoldings and signaling platforms. Cold Spring Harb. Perspect. Biol. 3, a004911. https://doi.org/10.1101/cshperspect.a004911.

10. Shinin, V., Gayraud-Morel, B., Gomès, D., and Tajbakhsh, S. (2006). Asymmetric division and cosegregation of template DNA strands in adult muscle satellite cells. Nat. Cell Biol. 8, 677–687. https://doi.org/10.1038/ncb1425.

11. Kuang, S., Kuroda, K., Le Grand, F., and Rudnicki, M.A. (2007). Asymmetric self-renewal and commitment of satellite stem cells in muscle. Cell 129, 999–1010. https://doi.org/10.1016/j.cell.2007.03.044.

12. Feige, P., Brun, C.E., Ritso, M., and Rudnicki, M.A. (2018). Orienting Muscle Stem Cells for Regeneration in Homeostasis, Aging, and Disease. Cell Stem Cell 23, 653–664. https://doi.org/10.1016/j.stem.2018.10.006.

13. Chargé, S.B., and Rudnicki, M.A. (2004). Cellular and molecular regulation of muscle regeneration. Physiol. Rev. 84, 209–238. https://doi.org/10.1152/physrev.00019.2003.

14. Bischoff, R., and Franzini-Armstrong, C. (2004). Satellite and Stem Cells in Muscle Regeneration. In Myology, A.G. Engel and C. Franzinin-Armstrong, eds. (McGraw-Hill).

15. Hardy, D., Besnard, A., Latil, M., Jouvion, G., Briand, D., Thépenier, C., Pascal, Q., Guguin, A., Gayraud-Morel, B., Cavaillon, J.M., et al. (2016). Comparative Study of Injury Models for Studying Muscle Regeneration in Mice. PLoS One 11, e0147198. https://doi.org/10.1371/journal.pone.0147198.

16. Caldwell, C.J., Mattey, D.L., and Weller, R.O. (1990). Role of the basement membrane in the regeneration of skeletal muscle. Neuropathol. Appl. Neurobiol. 16, 225–238. https://doi.org/10.1111/j.1365-2990.1990.tb01159.x.

17. Vracko, R., and Benditt, E.P. (1972). Basal lamina: the scaffold for orderly cell replacement. Observations on regeneration of injured skeletal muscle fibers and capillaries. J. Cell Biol. *55*, 406–419. https://doi.org/10.1083/jcb.55.2.406.

18. Schmalbruch, H. (1976). The morphology of regeneration of skeletal muscles in the rat. Tissue Cell *8*, 673–692. https://doi.org/10.1016/0040-8166(76)90039-2.

19. Sanes, J. (2004). The extracellular matrix. In Myology, A. Engel and C. Franzini-Armstrong, eds. (McGraw-Hill), pp. 471–487.

20. Lovering, R.M., Michaelson, L., and Ward, C.W. (2009). Malformed mdx myofibers have normal cytoskeletal architecture yet altered EC coupling and stress-induced Ca2+ signaling. Am. J. Physiol. Cell Physiol. *297*, C571–C580. https://doi.org/10.1152/ajpcell.00087.2009.

21. Head, S.I. (2010). Branched fibres in old dystrophic mdx muscle are associated with mechanical weakening of the sarcolemma, abnormal Ca2+ transients and a breakdown of Ca2+ homeostasis during fatigue. Exp. Physiol. *95*, 641–656. https://doi.org/10.1113/expphysiol.2009.052019.

22. Chan, S., Head, S.I., and Morley, J.W. (2007). Branched fibers in dystrophic mdx muscle are associated with a loss of force following lengthening contractions. Am. J. Physiol. Cell Physiol. *293*, C985–C992. https://doi.org/10.1152/ajpcell.00128.2007.

23. Chan, S., and Head, S.I. (2011). The role of branched fibres in the pathogenesis of Duchenne muscular dystrophy. Exp. Physiol. *96*, 564–571. https://doi.org/10.1113/expphysiol.2010.056713.

24. Pearce, G.W., and Walton, J.N. (1962). Progressive muscular dystrophy: the histopathological changes in skeletal muscle obtained by biopsy. J. Pathol. Bacteriol. *83*, 535–550. https://doi.org/10.1002/path.1700830228.

25. Bell, C.D., and Conen, P.E. (1968). Histopathological changes in Duchenne muscular dystrophy. J. Neurol. Sci. *7*, 529–544. https://doi.org/10.1016/0022-510x(68)90058-0.

26. Isaacs, E.R., Bradley, W.G., and Henderson, G. (1973). Longitudinal fibre splitting in muscular dystrophy: a serial cinematographic study. J. Neurol. Neurosurg. Psychiatry *36*, 813–819. https://doi.org/10.1136/jnnp.36.5.813.

27. Swash, M., and Schwartz, M.S. (1977). Implications of longitudinal muscle fibre splitting in neurogenic and myopathic disorders. J. Neurol. Neurosurg. Psychiatry *40*, 1152–1159. https://doi.org/10.1136/jnnp.40.12.1152.

28. Pichavant, C., and Pavlath, G.K. (2014). Incidence and severity of myofiber branching with regeneration and aging. Skelet. Muscle *4*, 9. https://doi.org/10.1186/2044-5040-4-9.

29. Ontell, M., and Feng, K.C. (1981). The three-dimensional cytoarchitecture and pattern of motor innervation of branched striated myotubes. Anat. Rec. *200*, 11–31. https://doi.org/10.1002/ar.1092000103.

30. Head, S.I., Stephenson, D.G., and Williams, D.A. (1990). Properties of enzymatically isolated skeletal fibres from mice with muscular dystrophy. J. Physiol. *422*, 351–367. https://doi.org/10.1113/jphysiol.1990.sp017988.

31. Ontell, M., Hughes, D., and Bourke, D. (1982). Secondary myogenesis of normal muscle produces abnormal myotubes. Anat. Rec. *204*, 199–207. https://doi.org/10.1002/ar.1092040304.

32. Clark, W.E. (1946). An experimental study of the regeneration of mammalian striped muscle. J. Anat. *80*, 24–36.4.

33. Meyer, G.A. (2018). Evidence of induced muscle regeneration persists for years in the mouse. Muscle Nerve *58*, 858–862. https://doi.org/10.1002/mus.26329.

34. Wada, K., Katsuta, S., and Soya, H. (2008). Formation process and fate of the nuclear chain after injury in regenerated myofiber. Anat. Rec. (Hoboken) *291*, 122–128. https://doi.org/10.1002/ar.20626.

35. Newlands, S., Levitt, L.K., Robinson, C.S., Karpf, A.B., Hodgson, V.R., Wade, R.P., and Hardeman, E.C. (1998). Transcription occurs in pulses in muscle fibers. Genes Dev. *12*, 2748–2758. https://doi.org/10.1101/gad.12.17.2748.

36. Cadot, B., Gache, V., and Gomes, E.R. (2015). Moving and positioning the nucleus in skeletal muscle - one step at a time. Nucleus *6*, 373–381. https://doi.org/10.1080/19491034.2015.1090073.

37. Folker, E.S., and Baylies, M.K. (2013). Nuclear positioning in muscle development and disease. Front. Physiol. *4*, 363. https://doi.org/10.3389/fphys.2013.00363.

38. Roman, W., and Gomes, E.R. (2018). Nuclear positioning in skeletal muscle. Semin. Cell Dev. Biol. *82*, 51–56. https://doi.org/10.1016/j.semcdb.2017.11.005.

39. Murphy, M., and Kardon, G. (2011). Origin of vertebrate limb muscle: the role of progenitor and myoblast populations. Curr. Top. Dev. Biol. *96*, 1–32. https://doi.org/10.1016/B978-0-12-385940-2.00001-2.

40. Musarò, A. (2014). The Basis of Muscle Regeneration. Adv. Biol. *2014*, 1–16. https://doi.org/10.1155/2014/612471.

41. Verma, M., Asakura, Y., Murakonda, B.S.R., Pengo, T., Latroche, C., Chazaud, B., McLoon, L.K., and Asakura, A. (2018). Muscle Satellite Cell Cross-Talk with a Vascular Niche Maintains Quiescence via VEGF and Notch Signaling. Cell Stem Cell *23*, 530–543.e9. https://doi.org/10.1016/j.stem.2018.09.007.

42. Muzumdar, M.D., Tasic, B., Miyamichi, K., Li, L., and Luo, L. (2007). A global double-fluorescent Cre reporter mouse. Genesis *45*, 593–605. https://doi.org/10.1002/dvg.20335.

43. Webster, M.T., Manor, U., Lippincott-Schwartz, J., and Fan, C.M. (2016). Intravital Imaging Reveals Ghost Fibers as Architectural Units Guiding Myogenic Progenitors during Regeneration. Cell Stem Cell *18*, 243–252. https://doi.org/10.1016/j.stem.2015.11.005.

44. Morton, A.B., Norton, C.E., Jacobsen, N.L., Fernando, C.A., Cornelison, D.D.W., and Segal, S.S. (2019). Barium chloride injures myofibers through calcium-induced proteolysis with fragmentation of motor nerves and microvessels. Skelet. Muscle *9*, 27. https://doi.org/10.1186/s13395-019-0213-2.

45. Schüler, S.C., Liu, Y., Dumontier, S., Grandbois, M., Le Moal, E., Cornelison, D., and Bentzinger, C.F. (2022). Extracellular matrix: Brick and mortar in the skeletal muscle stem cell niche. Front. Cell Dev. Biol. *10*, 1056523. https://doi.org/10.3389/fcell.2022.1056523.

46. Loreti, M., and Sacco, A. (2022). The jam session between muscle stem cells and the extracellular matrix in the tissue microenvironment. NPJ Regen. Med. *7*, 16. https://doi.org/10.1038/s41536-022-00204-z.

47. Wan, Y., Otsuna, H., Chien, C.B., and Hansen, C. (2009). An interactive visualization tool for multi-channel confocal microscopy data in neurobiology research. IEEE Trans. Vis. Comput. Graph. *15*, 1489–1496. https://doi.org/10.1109/TVCG.2009.118.

48. Moo, E.K., Fortuna, R., Sibole, S.C., Abusara, Z., and Herzog, W. (2016). In vivo Sarcomere Lengths and Sarcomere Elongations Are Not Uniform across an Intact Muscle. Front. Physiol. *7*, 187. https://doi.org/10.3389/fphys.2016.00187.

49. Christov, C., Chrétien, F., Abou-Khalil, R., Bassez, G., Vallet, G., Authier, F.J., Bassaglia, Y., Shinin, V., Tajbakhsh, S., Chazaud, B., et al. (2007). Muscle satellite cells and endothelial cells: close neighbors and privileged partners. Mol. Biol. Cell *18*, 1397–1409. https://doi.org/10.1091/mbc.E06-08-0693.

50. Muir, A.R., Kanji, A.H., and Allbrook, D. (1965). The structure of the satellite cells in skeletal muscle. J. Anat. *99*, 435–444.

51. Yin, H., Price, F., and Rudnicki, M.A. (2013). Satellite cells and the muscle stem cell niche. Physiol. Rev. *93*, 23–67. https://doi.org/10.1152/physrev.00043.2011.

52. Schmalbruch, H. (1978). Satellite cells of rat muscles as studied by freeze-fracturing. Anat. Rec. *191*, 371–376. https://doi.org/10.1002/ar.1091910309.

53. Haroon, M., Klein-Nulend, J., Bakker, A.D., Jin, J., Seddiqi, H., Offringa, C., de Wit, G.M.J., Le Grand, F., Giordani, L., Liu, K.J., et al. (2021). Myofiber stretch induces tensile and shear deformation of muscle stem cells in their native niche. Biophys. J. *120*, 2665–2678. https://doi.org/10.1016/j.bpj.2021.05.021.

54. Kann, A.P., Hung, M., Wang, W., Nguyen, J., Gilbert, P.M., Wu, Z., and Krauss, R.S. (2022). An injury-responsive Rac-to-Rho GTPase switch drives activation of muscle stem cells through rapid cytoskeletal remodeling. Cell Stem Cell *29*, 933–947.e6. https://doi.org/10.1016/j.stem.2022.04.016.

Developmental Cell
Article

CellPress

55. Ma, N., Chen, D., Lee, J.H., Kuri, P., Hernandez, E.B., Kocan, J., Mahmood, H., Tichy, E.D., Rompolas, P., and Mourkioti, F. (2022). Piezo1 regulates the regenerative capacity of skeletal muscles via orchestration of stem cell morphological states. Sci. Adv. 8, eabn0485. https://doi.org/10.1126/sciadv.abn0485.

56. Rodgers, J.T., King, K.Y., Brett, J.O., Cromie, M.J., Charville, G.W., Maguire, K.K., Brunson, C., Mastey, N., Liu, L., Tsai, C.R., et al. (2014). mTORC1 controls the adaptive transition of quiescent stem cells from G0 to G(Alert). Nature 510, 393–396. https://doi.org/10.1038/nature13255.

57. Siegel, A.L., Atchison, K., Fisher, K.E., Davis, G.E., and Cornelison, D.D. (2009). 3D timelapse analysis of muscle satellite cell motility. Stem Cells 27, 2527–2538. https://doi.org/10.1002/stem.178.

58. Rocheteau, P., Gayraud-Morel, B., Siegl-Cachedenier, I., Blasco, M.A., and Tajbakhsh, S. (2012). A subpopulation of adult skeletal muscle stem cells retains all template DNA strands after cell division. Cell 148, 112–125. https://doi.org/10.1016/j.cell.2011.11.049.

59. Dumont, N.A., Wang, Y.X., von Maltzahn, J., Pasut, A., Bentzinger, C.F., Brun, C.E., and Rudnicki, M.A. (2015). Dystrophin expression in muscle stem cells regulates their polarity and asymmetric division. Nat. Med. 21, 1455–1463. https://doi.org/10.1038/nm.3990.

60. Wang, Y.X., Feige, P., Brun, C.E., Hekmatnejad, B., Dumont, N.A., Renaud, J.M., Faulkes, S., Guindon, D.E., and Rudnicki, M.A. (2019). EGFR-Aurka Signaling Rescues Polarity and Regeneration Defects in Dystrophin-Deficient Muscle Stem Cells by Increasing Asymmetric Divisions. Cell Stem Cell 24, 419–432.e6. https://doi.org/10.1016/j.stem.2019.01.002.

61. Landing, B.H., Dixon, L.G., and Wells, T.R. (1974). Studies on isolated human skeletal muscle fibers, including a proposed pattern of nuclear distribution and a concept of nuclear territories. Hum. Pathol. 5, 441–461. https://doi.org/10.1016/s0046-8177(74)80023-7.

62. Pawlikowski, B., Pulliam, C., Betta, N.D., Kardon, G., and Olwin, B.B. (2015). Pervasive satellite cell contribution to uninjured adult muscle fibers. Skelet. Muscle 5, 42. https://doi.org/10.1186/s13395-015-0067-1.

63. Troy, A., Cadwallader, A.B., Fedorov, Y., Tyner, K., Tanaka, K.K., and Olwin, B.B. (2012). Coordination of satellite cell activation and self-renewal by Par-complex-dependent asymmetric activation of p38 α/β MAPK. Cell Stem Cell 11, 541–553. https://doi.org/10.1016/j.stem.2012.05.025.

64. Cutler, A.A., Pawlikowski, B., Wheeler, J.R., Dalla Betta, N., Elston, T., O'Rourke, R., Jones, K., and Olwin, B.B. (2022). The regenerating skeletal muscle niche drives satellite cell return to quiescence. iScience 25, 104444. https://doi.org/10.1016/j.isci.2022.104444.

65. Evano, B., Khalilian, S., Le Carrou, G., Almouzni, G., and Tajbakhsh, S. (2020). Dynamics of Asymmetric and Symmetric Divisions of Muscle Stem Cells In Vivo and on Artificial Niches. Cell Rep. 30, 3195–3206.e7. https://doi.org/10.1016/j.celrep.2020.01.097.

66. Rubinstein, N.A., and Kelly, A.M. (2004). The Diversity of Muscle Fiber Types and Its Origin During Development. In Myology, A.G. Engel and C. Franzini-Armstrong, eds. (McGraw-Hill), pp. 87–103.

67. Roman, W., Martins, J.P., Carvalho, F.A., Voituriez, R., Abella, J.V.G., Santos, N.C., Cadot, B., Way, M., and Gomes, E.R. (2017). Myofibril contraction and crosslinking drive nuclear movement to the periphery of skeletal muscle. Nat. Cell Biol. 19, 1189–1201. https://doi.org/10.1038/ncb3605.

68. Biressi, S., Molinaro, M., and Cossu, G. (2007). Cellular heterogeneity during vertebrate skeletal muscle development. Dev. Biol. 308, 281–293. https://doi.org/10.1016/j.ydbio.2007.06.006.

69. Hutcheson, D.A., Zhao, J., Merrell, A., Haldar, M., and Kardon, G. (2009). Embryonic and fetal limb myogenic cells are derived from developmentally distinct progenitors and have different requirements for beta-catenin. Genes Dev. 23, 997–1013. https://doi.org/10.1101/gad.1769009.

70. Juban, G., and Chazaud, B. (2021). Efferocytosis during Skeletal Muscle Regeneration. Cells 10, 3267. https://doi.org/10.3390/cells10123267.

71. Chazaud, B. (2020). Inflammation and Skeletal Muscle Regeneration: Leave It to the Macrophages! Trends Immunol. 41, 481–492. https://doi.org/10.1016/j.it.2020.04.006.

72. Tidball, J.G. (2017). Regulation of muscle growth and regeneration by the immune system. Nat. Rev. Immunol. 17, 165–178. https://doi.org/10.1038/nri.2016.150.

73. Tidball, J.G., and Villalta, S.A. (2010). Regulatory interactions between muscle and the immune system during muscle regeneration. Am. J. Physiol. Regul. Integr. Comp. Physiol. 298, R1173–R1187. https://doi.org/10.1152/ajpregu.00735.2009.

74. Arnold, L., Henry, A., Poron, F., Baba-Amer, Y., van Rooijen, N., Plonquet, A., Gherardi, R.K., and Chazaud, B. (2007). Inflammatory monocytes recruited after skeletal muscle injury switch into antiinflammatory macrophages to support myogenesis. J. Exp. Med. 204, 1057–1069. https://doi.org/10.1084/jem.20070075.

75. Summan, M., Warren, G.L., Mercer, R.R., Chapman, R., Hulderman, T., Van Rooijen, N., and Simeonova, P.P. (2006). Macrophages and skeletal muscle regeneration: a clodronate-containing liposome depletion study. Am. J. Physiol. Regul. Integr. Comp. Physiol. 290, R1488–R1495. https://doi.org/10.1152/ajpregu.00465.2005.

76. Van Rooijen, N.V., and Sanders, A. (1994). Liposome mediated depletion of macrophages: mechanism of action, preparation of liposomes and applications. J. Immunol. Methods 174, 83–93. https://doi.org/10.1016/0022-1759(94)90012-4.

77. Kawanishi, N., Mizokami, T., Niihara, H., Yada, K., and Suzuki, K. (2016). Macrophage depletion by clodronate liposome attenuates muscle injury and inflammation following exhaustive exercise. Biochem. Biophys. Rep. 5, 146–151. https://doi.org/10.1016/j.bbrep.2015.11.022.

78. Condic, M.L., and Bentley, D. (1989). Removal of the basal lamina in vivo reveals growth cone-basal lamina adhesive interactions and axonal tension in grasshopper embryos. J. Neurosci. 9, 2678–2686. https://doi.org/10.1523/JNEUROSCI.09-08-02678.1989.

79. Takemoto, Y., Inaba, S., Zhang, L., Tsujikawa, K., Uezumi, A., and Fukada, S.I. (2019). Implication of basal lamina dependency in survival of Nrf2-null muscle stem cells via an antioxidative-independent mechanism. J. Cell. Physiol. 234, 1689–1698. https://doi.org/10.1002/jcp.27040.

80. Watt, D.J., Morgan, J.E., Clifford, M.A., and Partridge, T.A. (1987). The movement of muscle precursor cells between adjacent regenerating muscles in the mouse. Anat. Embryol. (Berl) 175, 527–536. https://doi.org/10.1007/BF00309688.

81. Jockusch, H., and Voigt, S. (2003). Migration of adult myogenic precursor cells as revealed by GFP/nLacZ labelling of mouse transplantation chimeras. J. Cell Sci. 116, 1611–1616. https://doi.org/10.1242/jcs.00364.

82. Mackey, A.L., and Kjaer, M. (2017). The breaking and making of healthy adult human skeletal muscle in vivo. Skelet. Muscle 7, 24. https://doi.org/10.1186/s13395-017-0142-x.

83. Mao, Q., Acharya, A., Rodríguez-delaRosa, A., Marchiano, F., Dehapiot, B., Al Tanoury, Z., Rao, J., Díaz-Cuadros, M., Mansur, A., Wagner, E., et al. (2022). Tension-driven multi-scale self-organisation in human iPSC-derived muscle fibers. eLife 11, e76649. https://doi.org/10.7554/eLife.76649.

84. Dubowitz, V., and Sewry, C.A. (2007). Muscle Biopsy: A Practical Approach, Third Edition (Elsevier).

85. Silver, J.S., Günay, K.A., Cutler, A.A., Vogler, T.O., Brown, T.E., Pawlikowski, B.T., Bednarski, O.J., Bannister, K.L., Rogowski, C.J., McKay, A.G., et al. (2021). Injury-mediated stiffening persistently activates muscle stem cells through YAP and TAZ mechanotransduction. Sci. Adv. 7, eabe4501. https://doi.org/10.1126/sciadv.abe4501.

86. Carlson, B.M. (2005). Some principles of regeneration in mammalian systems. Anat. Rec. B New Anat. 287, 4–13. https://doi.org/10.1002/ar.b.20079.

87. Kiriaev, L., Kueh, S., Morley, J.W., North, K.N., Houweling, P.J., and Head, S.I. (2018). Branched fibers from old fast-twitch dystrophic muscles are the sites of terminal damage in muscular dystrophy. Am. J. Physiol. Cell Physiol. 314, C662–C674. https://doi.org/10.1152/ajpcell.00161.2017.

88. Hernández-Ochoa, E.O., Pratt, S.J.P., Garcia-Pelagio, K.P., Schneider, M.F., and Lovering, R.M. (2015). Disruption of action potential and

calcium signaling properties in malformed myofibers from dystrophin-deficient mice. Physiol. Rep. *3*, 3. https://doi.org/10.14814/phy2.12366.

89. Girardi, F., Taleb, A., Ebrahimi, M., Datye, A., Gamage, D.G., Peccate, C., Giordani, L., Millay, D.P., Gilbert, P.M., Cadot, B., et al. (2021). TGFbeta signaling curbs cell fusion and muscle regeneration. Nat. Commun. *12*, 750. https://doi.org/10.1038/s41467-020-20289-8.

90. Højfeldt, G., Sorenson, T., Gonzales, A., Kjaer, M., Andersen, J.L., and Mackey, A.L. (2023). Fusion of myofibre branches is a physiological feature of healthy human skeletal muscle regeneration. Skelet. Muscle *13*, 13. https://doi.org/10.1186/s13395-023-00322-2.

91. Griffin, C.A., Kafadar, K.A., and Pavlath, G.K. (2009). MOR23 promotes muscle regeneration and regulates cell adhesion and migration. Dev. Cell *17*, 649–661. https://doi.org/10.1016/j.devcel.2009.09.004.

92. Charrin, S., Latil, M., Soave, S., Polesskaya, A., Chrétien, F., Boucheix, C., and Rubinstein, E. (2013). Normal muscle regeneration requires tight control of muscle cell fusion by tetraspanins CD9 and CD81. Nat. Commun. *4*, 1674. https://doi.org/10.1038/ncomms2675.

93. Kanagawa, M., and Toda, T. (2006). The genetic and molecular basis of muscular dystrophy: roles of cell-matrix linkage in the pathogenesis. J. Hum. Genet. *51*, 915–926. https://doi.org/10.1007/s10038-006-0056-7.

94. Millay, D.P. (2022). Regulation of the myoblast fusion reaction for muscle development, regeneration, and adaptations. Exp. Cell Res. *415*, 113134. https://doi.org/10.1016/j.yexcr.2022.113134.

95. Wallace, G.Q., and McNally, E.M. (2009). Mechanisms of muscle degeneration, regeneration, and repair in the muscular dystrophies. Annu. Rev. Physiol. *71*, 37–57. https://doi.org/10.1146/annurev.physiol.010908.163216.

96. Jacobsen, N.L., Morton, A.B., and Segal, S.S. (2023). Angiogenesis precedes myogenesis during regeneration following biopsy injury of skeletal muscle. Skelet. Muscle *13*, 3. https://doi.org/10.1186/s13395-023-00313-3.

97. Anderson, S.E., Han, W.M., Srinivasa, V., Mohiuddin, M., Ruehle, M.A., Moon, J.Y., Shin, E., San Emeterio, C.L., Ogle, M.E., Botchwey, E.A.,

et al. (2019). Determination of a Critical Size Threshold for Volumetric Muscle Loss in the Mouse Quadriceps. Tissue Eng. Part C Methods *25*, 59–70. https://doi.org/10.1089/ten.TEC.2018.0324.

98. Filippone, C., Legros, V., Jeannin, P., Choumet, V., Butler-Browne, G., Zoladek, J., Mouly, V., Gessain, A., and Ceccaldi, P.E. (2020). Arboviruses and Muscle Disorders: From Disease to Cell Biology. Viruses *12*, 616. https://doi.org/10.3390/v12060616.

99. Rosenberg, A.S., Puig, M., Nagaraju, K., Hoffman, E.P., Villalta, S.A., Rao, V.A., Wakefield, L.M., and Woodcock, J. (2015). Immune-mediated pathology in Duchenne muscular dystrophy. Sci. Transl. Med. *7*, 299rv4. https://doi.org/10.1126/scitranslmed.aaa7322.

100. Batt, J.A., and Bain, J.R. (2013). Tibial nerve transection - a standardized model for denervation-induced skeletal muscle atrophy in mice. J. Vis. Exp. e50657. https://doi.org/10.3791/50657.

101. Dalkin, W., Taetzsch, T., and Valdez, G. (2016). The Fibular Nerve Injury Method: A Reliable Assay to Identify and Test Factors That Repair Neuromuscular Junctions. J. Vis. Exp. 54186. https://doi.org/10.3791/54186.

102. Greising, S.M., Baltgalvis, K.A., Kosir, A.M., Moran, A.L., Warren, G.L., and Lowe, D.A. (2011). Estradiol's beneficial effect on murine muscle function is independent of muscle activity. J. Appl. Physiol. (1985) *110*, 109–115. https://doi.org/10.1152/japplphysiol.00852.2010.

103. Murphy, M., Keefe, A., Lawson, J., Flygare, S., Yandell, M., and Kardon, G. (2014). Transiently active Wnt/β-catenin signaling is not required but must be silenced for stem cell function during muscle regeneration. Stem Cell Rep. *3*, 475–488. https://doi.org/10.1016/j.stemcr.2014.06.019.

104. Chi, J., Crane, A., Wu, Z., and Cohen, P. (2018). Adipo-Clear: A Tissue Clearing Method for Three-Dimensional Imaging of Adipose Tissue. J. Vis. Exp. 58271. https://doi.org/10.3791/58271.

Developmental Cell
Article

CellPress

STAR★METHODS

KEY RESOURCES TABLE

REAGENT or RESOURCE	SOURCE	IDENTIFIER
Antibodies		
Rabbit anti-mouse laminin antibody	Sigma Aldrich	Cat# L9393; RRID: AB_477163
Rat anti-mouse CD68 (clone FA-11) antibody	BioRad	Cat# MCA1957
Rabbit anti-DsRed antibody	Takara	Cat# 632496; RRID: AB_10013483
Chicken anti-green fluorescent protein antibody	Aves Labs	Cat# GFP-1010; RRID: AB_2307313
Mouse anti-MyHC (I, II, perinatal) (clone My32)	Sigma	Cat# M4276; RRID: AB_477190
Rat anti-mouse Itga7 647 (clone R2F2)	AbLab	Cat# 67-0010-05
Rat anti-mouse CD31 (PECAM-1), eFluor450 (clone 390)	eBioscience	Cat# 48-0311-82
Rat anti-mouse CD45, PerCp-Cyanine5.5 (clone 30-F11)	eBioscience	Cat# 45-0451-82
Rat anti-mouse CD45, eFluor450	eBioscience	Cat# 48-0451-80
Rat anti-mouse Ly-6A/E (Sca-1), PE-Cyanine7 (clone D7)	eBioscience	Cat# 25-5981-81
Rat anti-mouse F4/80, APC-eFluor780 (clone BM8)	eBioscience	Cat# 47-4801-82
Rat anti-mouse CD11b, APC (clone M1/70)	eBioscience	Cat# 17-0112-83
Rat anti-mouse CD16/CD32	eBioscience	Cat# 14-0161-85
AffiniPure Fab Fragment goat anti-mouse IgG (H+L)	Jackson ImmunoResearch	Cat# 115-007-003; RRID: AB_2338476
Alexa Fluor 647 AffiniPure Fab Fragment goat anti-rat IgG (H+L)	Jackson ImmunoResearch	Cat# 112-606-143; RRID: AB_2338412
Alexa Fluor 647 AffiniPure Fab Fragement goat anti-rabbit IgG (H+L)	Jackson ImmunoResearch	Cat# 111-606-144; RRID: AB_2307325
Alexa Fluor 594 AffiniPure goat anti-rabbit IgG (H+L)	Jackson ImmunoResearch	Cat# 111-585-144; RRID: AB_2307325
Alexa Fluor 488 AffiniPure goat anti-chicken IgY (IgG) Fc Fragment Specific	Jackson ImmunoResearch	Cat# 103-547-008; RRID: AB_2632424
Alexa Fluor 488 AffiniPure goat anti-chicken IgY (IgG) (H+L)	Jackson ImmunoResearch	Cat# 103-545-155: RRID: AB_2337390
Chemicals, peptides, and recombinant proteins		
Tamoxifen (TAM)	Cayman Chemical	Cat# 13258
Horse Serum	Gibco	Cat# 16050-122
Gentamicin (50mg/ml)	ThermoFisher Scientific	Cat# 15750060
Ham's/ F12 Nutrient Mix	ThermoFisher Scientific	Cat# 11765054
Macrophage depletion kit	Encapsula Nanosciences	Cat# CLD-8901
Liberase, Research Grade	Sigma Aldrich	Cat# 5401127001
DNAse I Recombinant, RNAse-free solution	Sigma Aldrich	Cat# 4716728001
EdU (5-ethynyl-2'-deoxyuridine)	ThermoFisher Scientific	Cat# A10044
Taq DNA Polymerase with ThermoPol Buffer	NEB	Cat# M0267L
100mM dNTP	ThermoFisher Scientific	Cat# 10297018
Histodenz	Sigma Aldrich	Cat# D2158-100G
VA-044	Wako Chemical USA	Cat# 011-19365
N,N,N',N'-tetrakis ethylenadiamine	Sigma Aldrich	Cat# H2383
Urea	Bio-Rad	Cat# 1610731
Boric Acid	Sigma Aldrich	Cat# B6768
Sodium deoxycholate (NaDC)	Sigma Aldrich	Cat# D6750-100G
Sodium Azide (NaN$_3$)	Sigma Aldrich	Cat# S2002-25G
Corn oil	Sigma Aldrich	Cat# C8267
Dichloromethane	Sigma Aldrich	Cat# 270997-1L
Dibenzyl Ether	Sigma Aldrich	Cat# 10814-3KG
Tween-20	Sigma Aldrich	Cat# P7949-500ml

(Continued on next page)

Continued

REAGENT or RESOURCE	SOURCE	IDENTIFIER
Triton X-100	Sigma Aldrich	Cat# T8787-250ml
Dimethyl Sulfoxide, HPLC Grade (DMSO)	Fisher Scientific	Cat# D159-4
Goat Serum	ThermoFisher Scientific	Cat# 16210-072
DAPI	ThermoFisher Scientific	Cat# D1306
Critical commercial assays		
Click-IT EdU Cell Proliferation Kit for Imaging, Alexa Fluor 647 dye	ThermoFisher Scientific	Cat# C10340
AbC Total Compensation Beads	ThermoFisher Scientific	Cat# A10497
Flow Cytometry Size Calibration Kit	ThermoFisher Scientific	Cat# F13838
Experimental models: Organisms/strains		
Mouse: *C57/BL6*	Jackson Laboratories	JAX: 000664
Mouse: *B6.Cg-Pax7$^{tm1(cre/ERT2)Gaka}$/J*	Gabrielle Kardon	JAX: 017763
Mouse: *STOCK.Pax7$^{tm1(cre)Mrc}$/J*	Mario Capecchi	JAX: 010530
Mouse: B6.129-*Pax3$^{tm1(cre)Joe}$*/J	Jonathan Epstein	JAX: 005549
Mouse: B6.129(Cg)-*Gt(ROSA) 26Sor$^{tm4(ACTB-tdTomato,-EGFP)Luo}$*/J	Jackson Laboratories	JAX: 007676
Oligonucleotides		
Genotyping primers for *B6.Cg-Pax7$^{tm1(cre/ERT2)Gaka}$/J* Common F: GCTGCTGTTGATTACCTGGC WT R: CTGCACTGAGACAGGACCG MUT R: CAAAAGACGGCAATATGGTG	Integrated DNA Technologies	Custom DNA Oligo
Genotyping primers for *STOCK.Pax7$^{tm1(cre)Mrc}$/J* Common F: TCGGCCTTCTTCTAGGTTCTGCTC WT R: GCTCTGGATACACCTGAGTCT MUT R: GGATAGTGAAACAGGGGCAA	Integrated DNA Technologies	Custom DNA Oligo
Genotyping primers for B6.129-*Pax3$^{tm1(cre)Joe}$*/J F: GCAGAACCTGAAGATGTTCGC R: ACACCAGAGACGGAAATCCATC	Integrated DNA Technologies	Custom DNA Oligo
Genotyping primers for B6.129(Cg)-*Gt(ROSA) 26Sor$^{tm4(ACTB-tdTomato,-EGFP)Luo}$*/J Common F: AAAGTCGCTCTGAGTTGTTAT WT R: GGAGCGGGAGAAATGGATATG Rosa26 Insert R: CCACGCGGGCCATTTACCGTAAG	Integrated DNA Technologies	Custom DNA Oligo
Software and algorithms		
Prism 9	GraphPad	RRID: SCR_002798
FlowJo 10	FLOWJO, LLC	RRID: SCR_008520
FluoRender	SCI, University of Utah	RRID: SCR_014303
ImageJ	NIH	RRID:SCR_003070

RESOURCE AVAILABILITY

Lead contact
Further information and requests for resources and reagents should be directed to and will be fulfilled by the lead contact Gabrielle Kardon (gkardon@genetics.utah.edu).

Materials availability
This study did not generate new unique reagents.

Data and code availability
All data reported in this paper will be shared by the lead contact upon request.
    All original code and related data will be shared by the lead contact upon request.
    Any additional information required to reanalyze the data reported in this paper is available from the lead contact upon request.

Developmental Cell
Article

CellPress

EXPERIMENTAL MODEL AND STUDY PARTICIPANT DETAILS

Mice

Male and female 3-6 month *Pax7*[CreERT2][27] and *Rosa*[mTmG],[42] back-crossed on to *C57/BL6J* background, as well as wild-type *C57/BL6J* mice (purchased from Jackson Laboratory) were used for all experiments in accordance protocols approved by the Institutional Animal Care and Use Committee at the University of Utah. Mice were housed in a pathogen-free facility in individually ventilated cages, with food and water provided ad libitum. Room temperature was maintained at 23+/- 0.7°C with 20-35% humidity and lighting followed a 12-h light/dark cycle.

METHOD DETAILS

Tamoxifen, EdU, and Encapsome/Clodrosome injections

Tamoxifen (TAM, Cayman Chemical, 13258) doses of 2 mg were delivered by intraperitoneal injection. For EdU experiments 10μg/g body mass of EdU in PBS (ThermoFisher Scientific, A10044) was delivered by intraperitoneal injection. Peripheral monocytes and infiltrating macrophages were depleted by intraperitoneal injection of 150μl clodrosome (clodronate encapsulated liposome solution, Encapsula NanoSciences, CLD-8901), which causes selective apoptotic cell death of these phagocytic cells,[75,76] and controls were injected with encapsome (liposome solution without clodronate).

Muscle injury and basement membrane disruption

Barium chloride (25 μl 1.2% in sterile demineralized water) was injected into the TA or EDL via a Hamilton syringe, as in Murphy et al.[7] The basement membranes of TA myofibers were disrupted simultaneously with muscle injury by injecting 0.2% ficin (Sigma F6008) diluted in 1.2% BaCl$_2$ in sterile water.

Common peroneal nerve denervation

The common peroneal nerve was transected on the left hindlimb.[100–102] A small skin incision was made in the direction from spine to thigh, centering over sciatic notch, and extending along the femur perpendicular to the course of the common peroneal nerve. Superficial fascia was incised to expose the hamstring muscles and a small incision was made through the hamstrings to expose the common peroneal nerve where it proximally intersects with the tendon of the lateral head of the gastrocnemius tendon. A 6-0 sterile silk suture was used to tie a knot at the proximal end and another at the distal end of the exposed nerve. The nerve was cut below the knot closest to the knee and the rest of the nerve was retracted by suturing to the bicep femoris. The hamstrings and skin incisions were closed with 6-0 sterile silk sutures.

FACS analysis

Isolation of mononuclear myogenic cells and macrophages from the TA was performed as described previously.[103] TAs from *Pax7*[CreERT2/+]*;Rosa*[mTmG/+] mice were dissected, minced and digested for 1 h at 37°C in 100 μl of 5mg/ml liberase (Sigma Aldrich, 5401127001) and 25 μl of 10U/μl DNAseI (Sigma Aldrich, 4716728001) in 3 ml Ham's F12 media (ThermoFisher Scientific, 11765054). Samples were passed through 70um and 40um filters, spun at 1800 rpm for 10 min, supernatant aspirated, and pellet resuspended in SC growth media: 15% horse serum (Gibco, 16050-122), 1:1000 50mg/ml gentamicin (ThermoFisher Scientific, 15750060) in F12 media. Myogenic mononuclear cells were isolated via GFP. If needed, cells were incubated with Fc receptor CD16/CD32 (eBioscience, 14-0161-85) then stained with an antibody mixture of eFluor450 rat anti-mouse CD31(clone 390), PerCp-Cy5.5 rat anti-mouse CD45 (clone 30-F11), PeCy7 rat anti-mouse Sca-1 (clone D7), APC-eFluour780 rat anti-mouse F4/80 (clone BM8) and APC rat anti-mouse CD11b (clone M1/70) from eBiosciences, and Itga7 647 (clone R2F2) from AbLab (see key resources table). Samples were incubated with antibodies on ice for 60 min, washed, and resuspended with SC growth media + DAPI for FACS analysis on the FACSAria III (BD Biosciences). Total mononuclear GFP+ myogenic cells (DAPI, TOM- negative, GFP+ or CD31-,CD45-, TOM-, GFP+) (Figure S1) and total macrophages (CD31-, CD45+, F4/80+, CD11b+) were calculated from entirely drained TA samples (Figure S1). GFP+ cell diameter was measured using the flow cytometry size calibration kit from ThermoFisher Scientific.

Myofiber preps

EDL muscles were isolated and incubated in 400U Collagenase Type 1 (Worthington LS004196) diluted in F12 for 100 min at 37C, individual myofibers were shaken off in a 10 cm plate and then individually transferred to a new plate with Ca, Mg-free PBS. Myofibers were fixed in 4% PFA, washed in PBS, and then individually mounted on slides for confocal imaging.

Muscle clearing for whole-mount imaging of endogenous fluorescence

The following protocol was adapted from Verma et al.[41] Mice were anesthetized with an overdose of isoflurane and an intracardiac perfusion and fixation was performed with PBS followed by 2% PFA. Harvested EDL samples were post-fixed in 2% PFA at 4°C 4 hours (H) - overnight. Fixed samples were washed 3 x 30 min in PBSTT: PBS with 0.1% Triton X-100 (Sigma Aldrich, T8787) and 0.1% Tween-20 (Sigma Aldrich, P7949). Samples were incubated in 4% acrylamide solution with 0.25% of thermal initiator VA-044 (Wako Chemical, 011-19365) for 4H rocking at 4°C. Samples were polymerized by incubated in fresh, degassed acrylamide solution for

CellPress

Developmental Cell
Article

3-4 H rotating at 37°C. The polymerized samples were washed 3 x 30 min with PBSTT at 37°C. Samples were then incubated in clearing solution (pH 9.3) containing 10% N,N,N',N'-tetrakis ethylenadiamine (Sigma-Aldrich, H2383), 10% Urea (Bio-Rad, 1610731), 5% Triton X-100, 5% sodium deoxycholate (Sigma Aldrich, D6750), and 20mM boric acid (Sigma Aldrich, B6768) rotating overnight at 37°C. Prior to mounting samples for confocal imaging, the refractive index of the tissue was matched using 88% Histodenz in PBSTT (Sigma Aldrich D2158) with 0.01% w/v sodium azide (Sigma Aldrich S2002) overnight at RT. Samples were submerged in 88% Histodenz solution in a well slide for imaging. Samples were protected from light during the entire protocol.

Whole-mount immunostaining
GFP, TOM, Laminin, Myosin, and EdU
After the modified muscle tissue clearing protocol from Verma et al.,[41] samples were washed extensively in PBS at RT and then incubated 1H at RT in blocking solution containing 5% goat serum (ThermoFisher Scientific, 16210-072), 20% DMSO (Fisher Scientific, D159-4) in PBS with anti-mouse Fab fragments (Jackson ImmunoResearch, 115-007-003) added if needed. Then samples were incubated with primary antibodies diluted in 5% goat serum and 20% DMSO in PBS for 2 days at RT; primary antibodies included GFP (1:500; Aves Labs, GFP-1010), and dsRed (1:200; Takara, 632496), laminin (1:100; Sigma Aldrich, L9393), and Myosin Heavy Chain (1:000 Sigma Aldrich M4276). Samples were washed extensively with PBS and then incubated in secondary antibody diluted in 5% goat serum and 20% DMSO in PBS for 3 days at RT in the dark; secondary antibodies were conjugated with Alexa 488, Alexa 594, or Alexa 647 (Jackson ImmunoResearch; see key resources table). Samples were washed extensively in PBS and stored at 4°C in the dark until imaging. Samples were washed 3 x 30 min with PBSTT prior to incubation in Histodenz solution.

Samples labeled with EdU were additionally blocked in 3% BSA in PBS for 15 min at RT and then underwent the Click-it reaction at 37°C according to manufacturer's protocol. Click-it reaction was quenched with 15 min of 3% BSA in PBS followed by extensive PBSTT washes at RT.

CD68
The following protocol was adapted from Chi et al.[104] Mice were anesthetized with an overdose of isoflurane and an intracardiac perfusion and fixation was performed with PBS followed by 4% PFA. Harvested EDL samples were post-fixed in 4% PFA at 4°C 4H - overnight. Fixed samples were washed extensively in PBS and dehydrated with a series of 20%, 40%, 60%, 80% methanol in H_2O with 0.1% Triton X-100 and 0.3 M glycine (B1N buffer, pH 7) and 100% methanol washes for 30 min each at 4°C shaking. Samples were then delipidated in 100% dichloromethane (DCM, Sigma Aldrich, 270997) for 3 x 30 min at 4°C with shaking. Samples were washed with 100% methanol three times and then rehydrated in a reversed methanol/B1N series, 80% 60%, 40%, 20% for 30 min each at 4°C. Samples were then washed in B1N 2 x 30 min at RT and washed overnight in B1N at RT. Samples were permeabilized in PBS with 0.1% Triton X-100, 0.05% Tween20, and 2μg/ml heparin (PTwH) for 2 x 1H at RT. Samples were incubated in primary antibody in PTwH for 3 days at RT. The primary antibodies used with this protocol were GFP (1:500; Aves Labs, GFP-1010) and CD68 (1:100; Bio-Rad, MCA1957). Samples were washed extensively with PTwH and then incubated in secondary antibody diluted in PTwH for 3 days at RT in the dark; secondary antibodies were conjugated with Alexa 488 and Alexa 647 (Jackson ImmunoResearch; see key resources table). Samples were washed extensively in PTwH prior to tissue clearing. To clear the tissue, samples were dehydrated in 25%, 50%, 75%, 100%, 100%, methanol/H_2O series for 30 min each at RT. Following dehydration, samples were washed with 100% DCM for 30 min three times, followed by overnight clearing in dibenzyl ether (DBE; Sigma Aldrich, 10814) at RT. Samples were mounted submerged in 100% DBE in a welled slide for imaging

Whole-mount imaging and 3D rendering
Whole mount muscle samples were imaged on a Leica SP8 confocal microscope with PL APO 20x/0.75 and 63x/1.40 oil immersion objectives were used with Z optical sections of 3 μm and 1 μm, respectively. A linear increase in laser intensity was used for deeper tissue imaging. Isolated myofibers were imaged on an Nikon ARX with PL Apo 20X/0.80 objective with z optical sections of 1 um.

Optical stacks of images were rendered in depth mode with Fluorender.[47] To highlight objects (GFP+ cells, basement membrane, branched fibers), objects were selected in Fluorender using the paint brush tool on individual Z optical sections and objects were extracted, rendered and pseudo-colored.

Quantification of myogenic cell and BM morphology
Myogenic cell volume
In Fluorender GFP+ cells were selected using the paint brush tool on individual Z optical sections and extracted and the component analyzer tool was used to measure cell volume of the extracted cells.
SC projection number and length
In Fluorender individual GFP+cells were extracted and the polyline ruler tool was used measure projection length. Projections were measured from the nucleus to the tip of the longest branch; 3 μm was the minimum length required to be considered a projection. Because many projections split and have several terminal ends, branches longer than 3 μm were measured from the junction with the main projection to tip of the branch. The length of all the branches on one projection were summed to give the total projection length.
Myofiber diameter
In Fluorender, images of GFP+ regenerated myofibers were rotated to view myofibers in cross-section. Then images of cross-sections at multiple points along the length of the myofibers were obtained. These images were imported into Image J and myofiber diameter was measured using the line tool at each y-axis cross-section and averaged for each myofiber analyzed.

Developmental Cell
Article

CellPress

BM diameter

Using Fluorender, the diameter of 3D rendered images of laminin+ BM tubes were measured at multiple points along the length of the tubes using the ruler tool. Then the average diameter was calculated for each BM tube measured. At 2dpi, the widest and most constricted dimensions of BM tubes was measured with the ruler tool.

Branched fibers

To determine the percentage of branched regeneration fibers in each muscle sample, Z-stacks of the composite rendered images were scanned for branched regenerated GFP+ myofibers. If there were multiple branches on a single myofiber, this was still counted as one branched myofiber. Because there was variability in the number of regenerated myofibers between samples, myofiber branching was expressed as a percentage of total regenerated GFP+ myofibers. The total number of regenerated myofibers was counted on images rotated to visualize myofibers in cross-section.

QUANTIFICATION AND STATISTICAL ANALYSIS

Statistical analyses were performed using Prism 9 (Graphpad, La Jolla, CA). For comparison between two groups, unpaired t tests were used. For comparison between multiple groups, one-way ANOVA with multiple comparisons Holm-Sidak post-hoc analysis was used. An alpha level of 0.05 was used for all analyses. All values are displayed as means ± SEM. Asterisks (*), (**), (***), (****) indicate statistically significant differences between the compared values ($p < 0.05$, $p < 0.01$, $p < 0.001$ and $p < 0.0001$, respectively).